CHAPTER

15

REFLECTOR ANTENNAS

15.1 INTRODUCTION

Reflector antennas, in one form or another, have been in use since the discovery of electromagnetic wave propagation in 1888 by Hertz. However the fine art of analyzing and designing reflectors of many various geometrical shapes did not forge ahead until the days of World War II when numerous radar applications evolved. Subsequent demands of reflectors for use in radio astronomy, microwave communication, and satellite tracking resulted in spectacular progress in the development of sophisticated analytical and experimental techniques in shaping the reflector surfaces and optimizing illumination over their apertures so as to maximize the gain. The use of reflector antennas for deep space communication, such as in the space program and especially their deployment on the surface of the moon, resulted in establishing the reflector antenna almost as a household word during the 1960s. Although reflector antennas take many geometrical configurations, some of the most popular shapes are the plane, corner, and curved reflectors (especially the paraboloid), as shown in Figure 15.1, each of which will be discussed in this chapter. Many articles on various phases of the analysis and design of curved reflectors have been published and some of the most referenced can be found in a book of reprinted papers [1].

15.2 PLANE REFLECTOR

The simplest type of reflector is a plane reflector introduced to direct energy in a desired direction. The arrangement is that shown in Figure 15.1(a) which has been extensively analyzed in Section 4.7 when the radiating source is a vertical or horizontal linear element. It has been clearly demonstrated that the polarization of the radiating source and its position relative to the reflecting surface can be used to control the radiating properties (pattern, impedance, directivity) of the overall system. Image theory has been used to analyze the radiating characteristics of such a system. Although the infinite dimensions of the plane reflector are idealized, the results can be used as approximations for electrically large surfaces. The perturbations introduced by keeping the dimensions finite can be accounted for by using special methods such as the Geometrical Theory of Diffraction [2]–[5] which was introduced in Section 12.10.
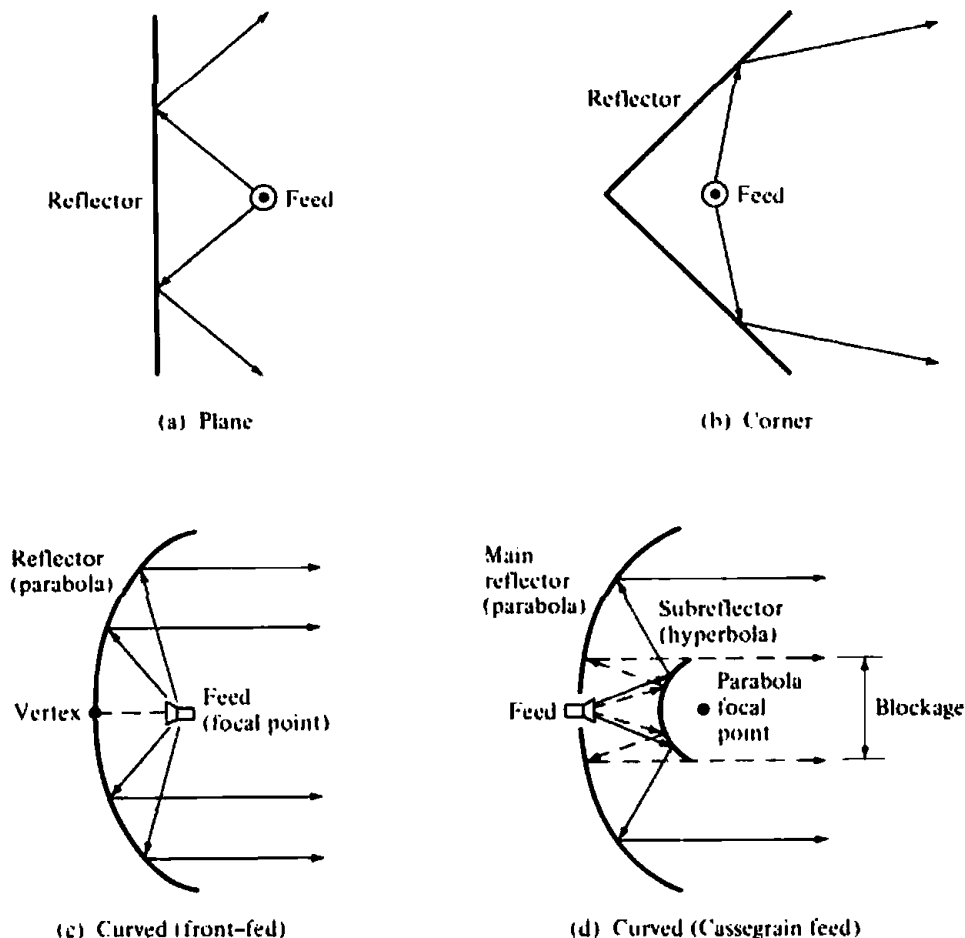
785

Reflector

Feed

(a) Plane

Reflector

Feed

(b) Corner

Reflector
(parabola)

Vertex

Feed
(focal point)

(c) Curved (front-fed)

Main
reflector
(parabola)

Subreflector
(hyperbola)

Parabola
focal
point

Blockage

Feed

(d) Curved (Cassegrain feed)

Figure 15.1 Geometrical configuration for some reflector systems.

15.3 CORNER REFLECTOR

To better collimate the energy in the forward direction, the geometrical shape of the plane reflector itself must be changed so as to prohibit radiation in the back and side directions. One arrangement which accomplishes that consists of two plane reflectors joined so as to form a corner, as shown in Figures 15.1(b) and in 15.2(a). This is known as the corner reflector. Because of its simplicity in construction, it has many unique applications. For example, if the reflector is used as a passive target for radar or communication applications, it will return the signal exactly in the same direction as it received it when its included angle is 90°. This is illustrated geometrically in Figure 15.2(b). Because of this unique feature, military ships and vehicles are designed with minimum sharp corners to reduce their detection by enemy radar. Corner reflectors are also widely used as receiving elements for home television.

In most practical applications, the included angle formed by the plates is usually 90°; however other angles are sometimes used. To maintain a given system efficiency, the spacing between the vertex and the feed element must increase as the included angle of the reflector decreases, and vice-versa. For reflectors with infinite sides, the gain increases as the included angle between the planes decreases. This, however, may not be true for finite size plates. For simplicity, in this chapter it will be assumed that the plates themselves are infinite in extent ($l = \infty$). However, since in practice the dimensions must be finite, guidelines on the size of the aperture (D_a), length (l), and height (h) will be given.

The feed element for a corner reflector is almost always a dipole or an array of

(a) Side view

(b) $\alpha = 90°$
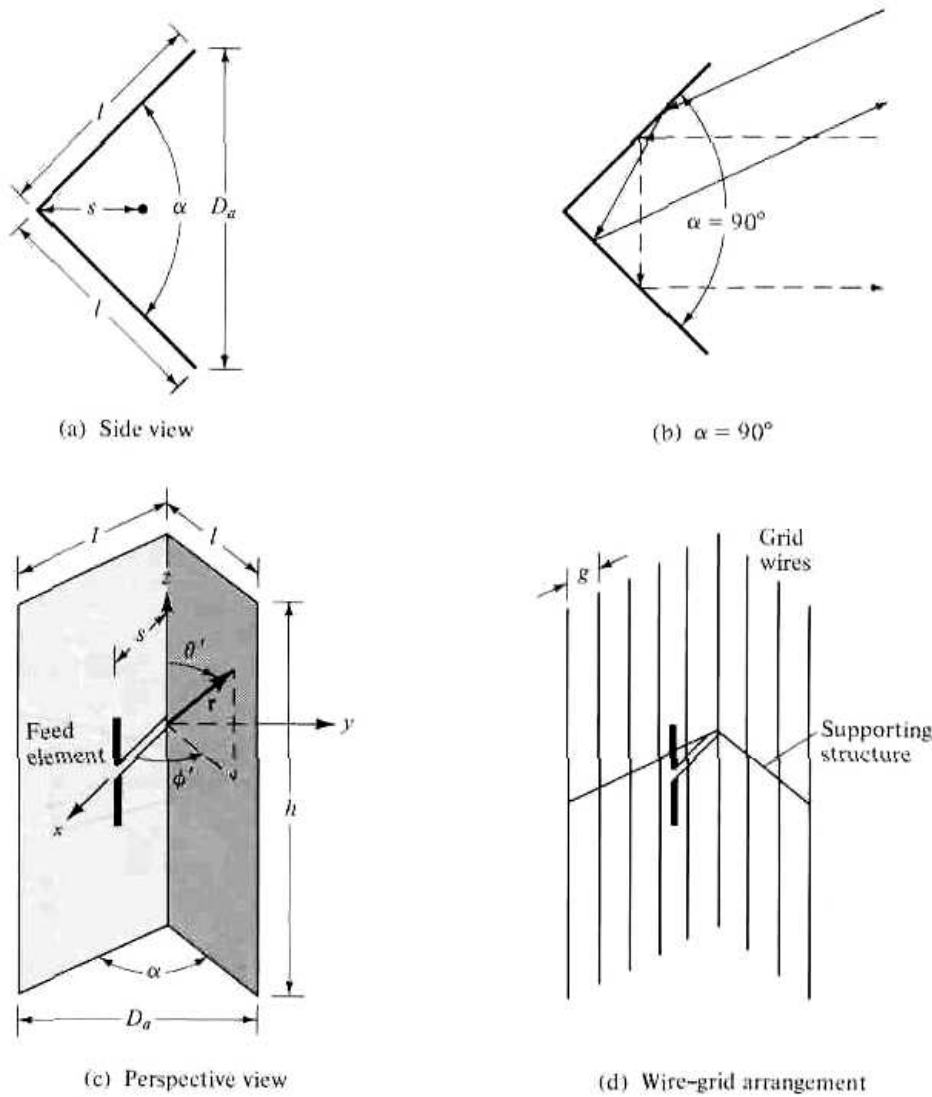
(c) Perspective view

(d) Wire-grid arrangement

Figure 15.2 Side and perspective views of solid and wire-grid corner reflectors.

collinear dipoles placed parallel to the vertex a distance s away, as shown in a perspective view in Figure 15.2(c). Greater bandwidth is obtained when the feed elements are cylindrical or biconical dipoles instead of thin wires. In many applications, especially when the wavelength is large compared to tolerable physical dimensions, the surfaces of the corner reflector are frequently made of grid wires rather than solid sheet metal, as shown in Figure 15.2(d). One of the reasons for doing that is to reduce wind resistance and overall system weight. The spacing (g) between wires is made a small fraction of a wavelength (usually $g \leq \lambda/10$). For wires that are parallel to the length of the dipole, as is the case for the arrangement of Figure 15.2(d), the reflectivity of the grid-wire surface is as good as that of a solid surface.

In practice, the aperture of the corner reflector (D_a) is usually made between one and two wavelengths ($\lambda < D_a < 2\lambda$). The length of the sides of a 90° corner reflector is most commonly taken to be about twice the distance from the vertex to the feed ($l \simeq 2s$). For reflectors with smaller included angles, the sides are made larger. The feed-to-vertex distance (s) is usually taken to be between $\lambda/3$ and $2\lambda/3$ ($\lambda/3 < s < 2\lambda/3$). For each reflector, there is an optimum feed-to-vertex spacing. If the spacing becomes too small, the radiation resistance decreases and becomes comparable to the loss resistance of the system which leads to an inefficient antenna. For very large spacing, the system produces undesirable multiple lobes, and it loses its directional
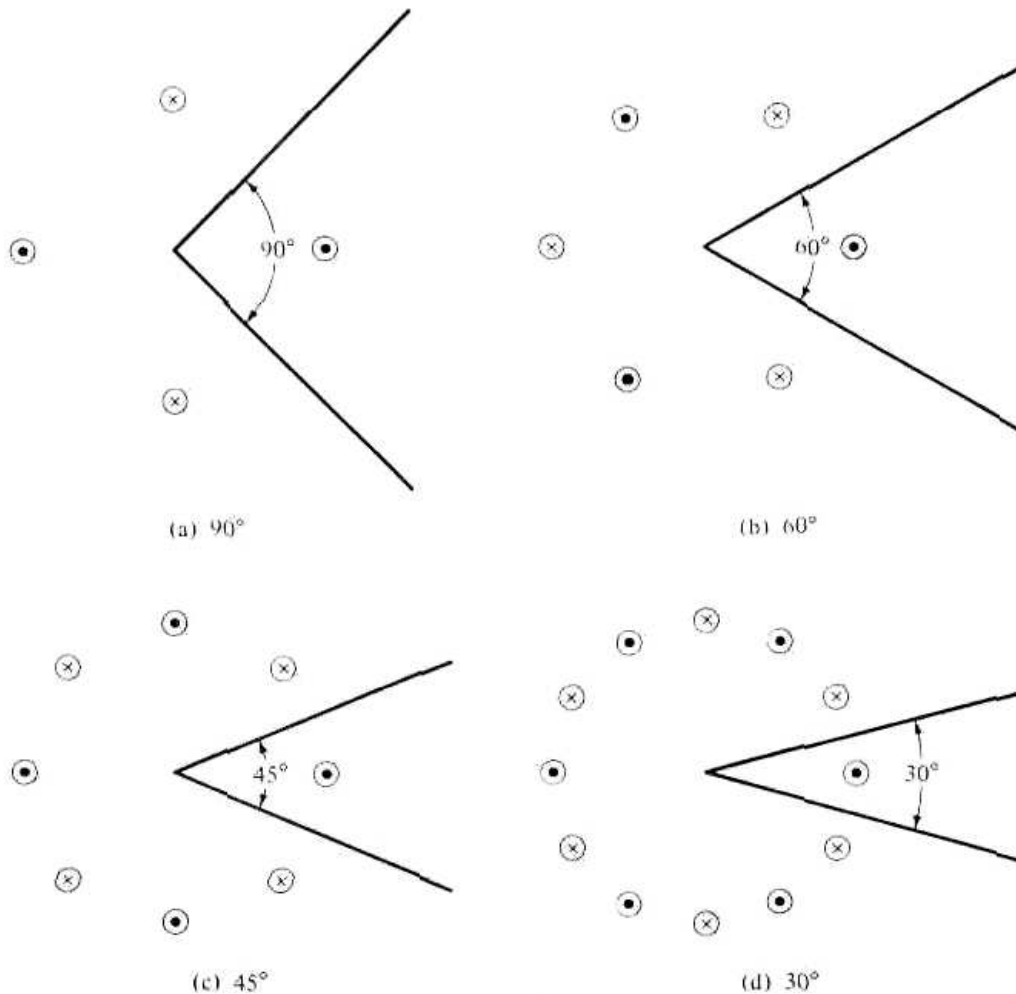
(a) 90°

(b) 60°

(c) 45°

(d) 30°

Figure 15.3   Corner reflectors and their images (with perpendicularly polarized feeds) for angles of 90°, 60°, 45°, and 30°.

characteristics. It has been experimentally observed that increasing the size of the sides does not greatly affect the beamwidth and directivity, but it increases the bandwidth and radiation resistance. The main lobe is somewhat broader for reflectors with finite sides compared to that of infinite dimensions. The height (h) of the reflector is usually taken to be about 1.2 to 1.5 times greater than the total length of the feed element, in order to reduce radiation toward the back region from the ends.

The analysis for the field radiated by a source in the presence of a corner reflector is facilitated when the included angle (α) of the reflector is $\alpha = \pi/n$, where n is an integer ($\alpha = \pi$, $\pi/2$, $\pi/3$, $\pi/4$, etc.). For those cases ($\alpha = 180°$, 90°, 60°, 45°, etc.) it is possible to find a system of images, which when properly placed in the absence of the reflector plates, form an array that yields the same field within the space formed by the reflector plates as the actual system. The number of images, polarity, and position of each is controlled by the included angle of the corner reflector and the polarization of the feed element. In Figure 15.3 we display the geometrical and electrical arrangement of the images for corner reflectors with included angles of 90°, 60°, 45°, and 30° and a feed with perpendicular polarization. The procedure for finding the number, location, and polarity of the images is demonstrated graphically in Figure 15.4 for a corner reflector with a 90° included angle. It is assumed that the feed element is a linear dipole placed parallel to the vertex. A similar procedure can be followed for all other reflectors with an included angle of $\alpha = 180°/n$, where n is an integer.

(a) 90° corner reflector

(b) Images for 90° corner reflector

(c) Placement of image #2 (due to feed)

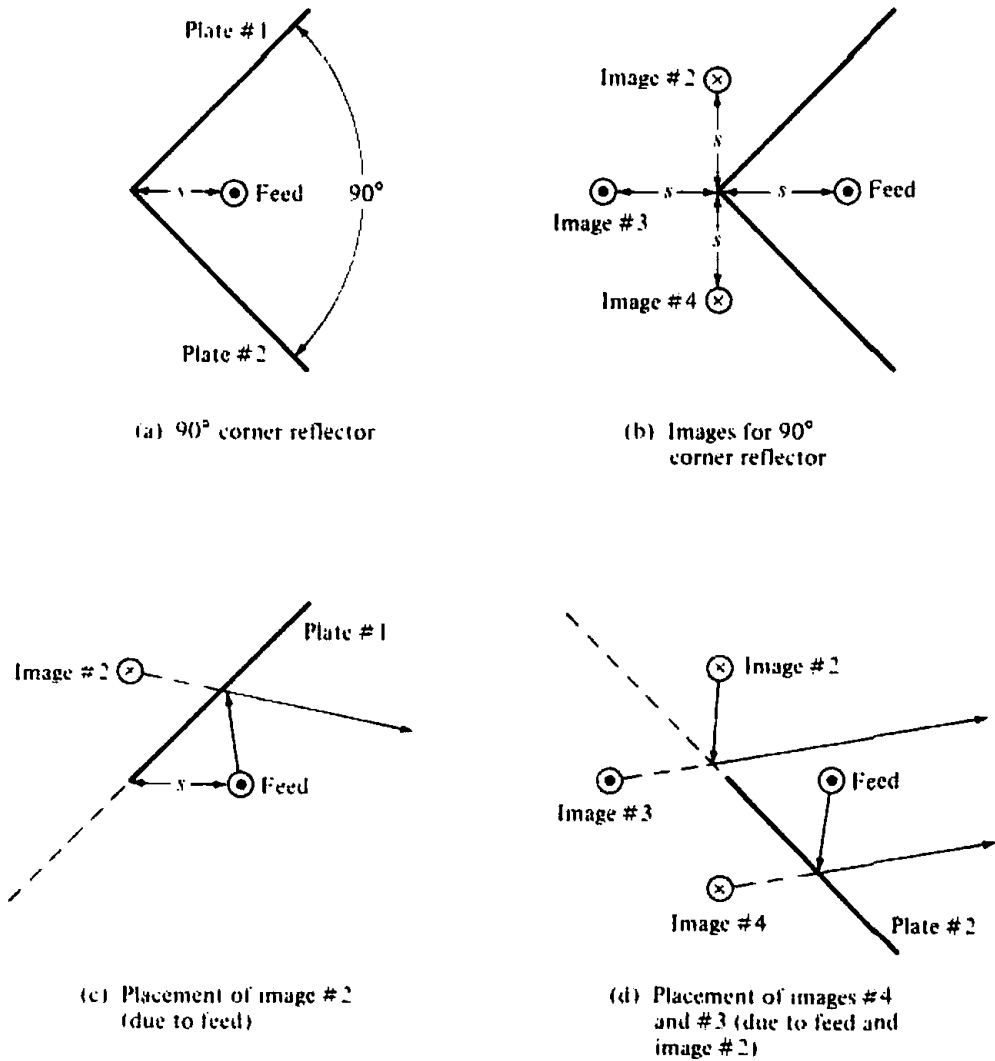(d) Placement of images #4 and #3 (due to feed and image #2)

Figure 15.4 Geometrical placement and electrical polarity of images for a 90° corner reflector with a parallel polarized feed.

15.3.1 90° Corner Reflector

The first corner reflector to be analyzed is the one with an included angle of 90°. Because its radiation characteristics are the most attractive, it has become the most popular.

Referring to the reflector of Figure 15.2(c) with its images in Figure 15.4(b), the total field of the system can be derived by summing the contributions from the feed and its images. Thus

$$E(r, \theta, \phi) = E_1(r_1, \theta, \phi) + E_2(r_2, \theta, \phi) + E_3(r_3, \theta, \phi) + E_4(r_4, \theta, \phi) \qquad (15\text{-}1)$$

In the far-zone, the normalized scalar field can be written as

$$E(r, \theta, \phi) = f(\theta, \phi)\frac{e^{-jkr_1}}{r_1} - f(\theta, \phi)\frac{e^{-jkr_2}}{r_2} + f(\theta, \phi)\frac{e^{-jkr_3}}{r_3} - f(\theta, \phi)\frac{e^{-jkr_4}}{r_4}$$

$$E(r, \theta, \phi) = [e^{+jks\cos\psi_1} - e^{+jks\cos\psi_2} + e^{+jks\cos\psi_3} - e^{+jks\cos\psi_4}] f(\theta, \phi)\frac{e^{-jkr}}{r} \qquad (15\text{-}2)$$

where

$$\cos \psi_1 = \hat{a}_x \cdot \hat{a}_r = \sin \theta \cos \phi \qquad \text{(15-2a)}$$

$$\cos \psi_2 = \hat{a}_y \cdot \hat{a}_r = \sin \theta \sin \phi \qquad \text{(15-2b)}$$

$$\cos \psi_3 = -\hat{a}_x \cdot \hat{a}_r = -\sin \theta \cos \phi \qquad \text{(15-2c)}$$

$$\cos \psi_4 = -\hat{a}_y \cdot \hat{a}_r = -\sin \theta \sin \phi \qquad \text{(15-2d)}$$

since $\hat{a}_r = \hat{a}_x \sin \theta \cos \phi + \hat{a}_y \sin \theta \sin \phi + \hat{a}_z \cos \theta$. Equation (15-2) can also be written, using (15-2a)–(15-2d), as

$$E(r, \theta, \phi) = 2[\cos(ks \sin \theta \cos \phi) - \cos(ks \sin \theta \sin \phi)] f(\theta, \phi) \frac{e^{-jkr}}{r} \qquad \text{(15-3)}$$

where for $\alpha = \pi/2 = 90°$

$$0 \le \theta \le \pi, \qquad \begin{array}{c} 0 \le \phi \le \alpha/2 \\[4pt] 2\pi - \alpha/2 \le \phi \le 2\pi \end{array} \qquad \text{(15-3a)}$$

Letting the field of a single isolated (radiating in free-space) element to be

$$E_0 = f(\theta, \phi) \frac{e^{-jkr}}{r} \qquad \text{(15-4)}$$

(15-3) can be rewritten as

$$\boxed{\frac{E}{E_0} = AF(\theta, \phi) = 2[\cos(ks \sin \theta \cos \phi) - \cos(ks \sin \theta \sin \phi)]} \qquad \text{(15-5)}$$

Equation (15-5) represents not only the ratio of the total field to that of an isolated element at the origin but also the array factor of the entire reflector system. In the azimuthal plane ($\theta = \pi/2$), (15-5) reduces to

$$\frac{E}{E_0} = AF(\theta = \pi/2, \phi) = 2[\cos(ks \cos \phi) - \cos(ks \sin \phi)] \qquad \text{(15-6)}$$

To gain some insight into the performance of a corner reflector, in Figure 15.5 we display the normalized patterns for an $\alpha = 90°$ corner reflector for spacings of $s = 0.1\lambda$, 0.7λ, 0.8λ, 0.9λ, and 1.0λ. It is evident that for the small spacings the pattern consists of a single major lobe whereas multiple lobes appear for the larger spacings ($s > 0.7\lambda$). For $s = \lambda$ the pattern exhibits two lobes separated by a null along the $\phi = 0°$ axis.

Another parameter of performance for the corner reflector is the field strength along the symmetry axis ($\theta = 90°$, $\phi = 0°$) as a function of feed-to-vertex distance s [6]. The normalized (relative to the field of a single isolated element) absolute field strength $|E/E_0|$ as a function of s/λ ($0 \le s \le 10\lambda$) for $\alpha = 90°$ is shown plotted in Figure 15.6. It is apparent that the first field strength peak is achieved when $s = 0.5\lambda$, and it is equal to 4. The field is also periodic with a period of $\Delta s/\lambda = 1$.

15.3.2 Other Corner Reflectors

A similar procedure can be used to derive the array factors and total fields for all other corner reflectors with included angles of $\alpha = 180°/n$. Referring to Figure 15.3, it can be shown that the array factors for $\alpha = 60°$, $45°$, and $30°$ can be written as

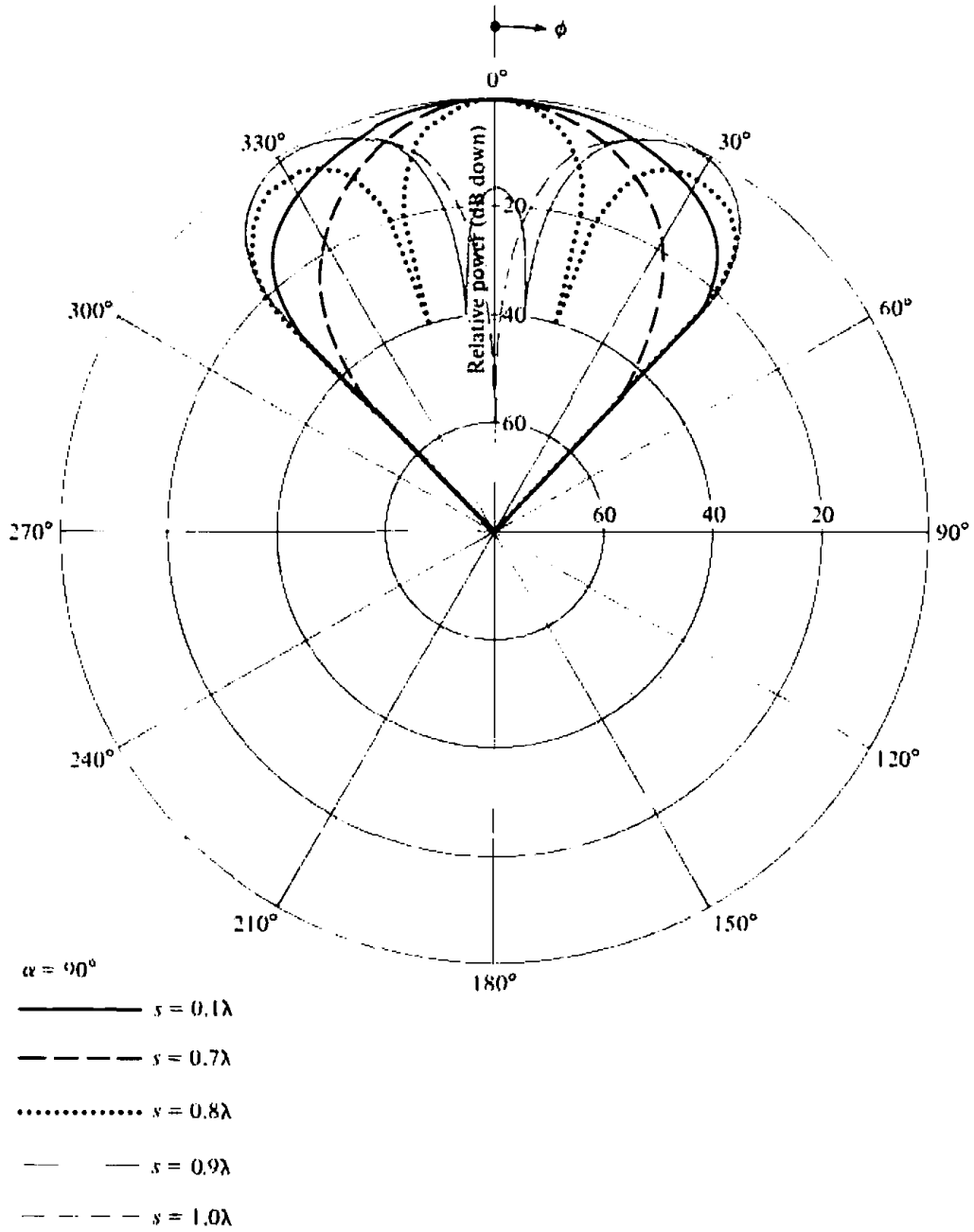**Figure 15.5** Normalized radiation amplitude patterns for $\alpha = 90°$ corner reflector.

$$\frac{\alpha = 60°}{AF(\theta, \phi) = 4 \sin\left(\frac{X}{2}\right) \left[\cos\left(\frac{X}{2}\right) - \cos\left(\sqrt{3}\,\frac{Y}{2}\right)\right]}$$

(15-7)

$$\frac{\alpha = 45°}{AF(\theta, \phi) = 2 \left[\cos(X) + \cos(Y) - 2\cos\left(\frac{X}{\sqrt{2}}\right)\cos\left(\frac{Y}{\sqrt{2}}\right)\right]}$$
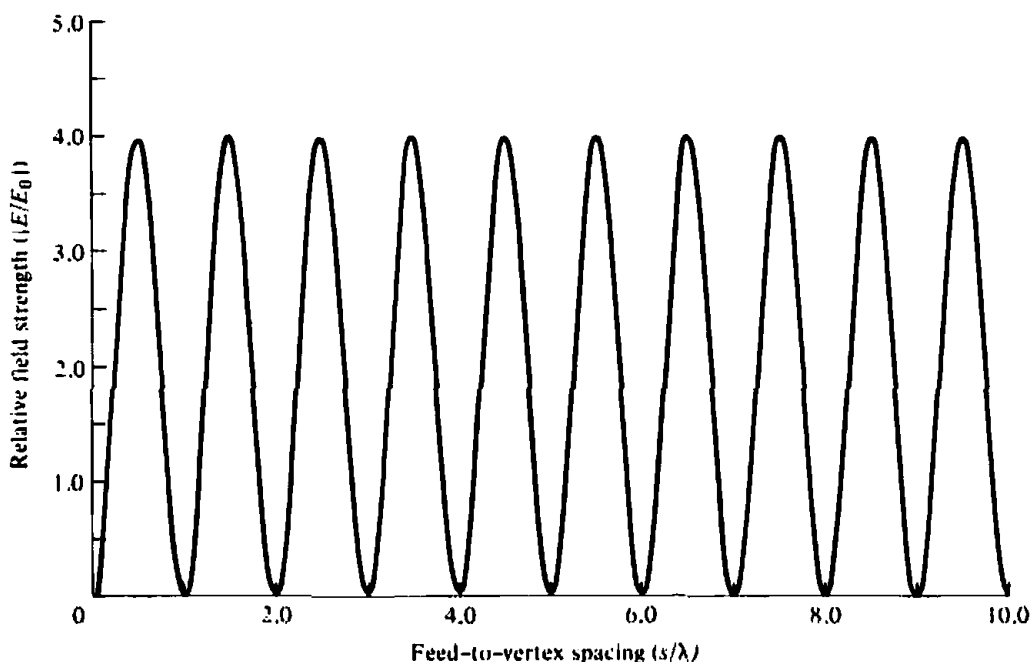
(15-8)

Figure 15.6   Relative field strength along the axis ($\theta = 90°$, $\phi = 0°$) of an $\alpha = 90°$ corner reflector as a function of feed-to-vertex spacing.

$$\alpha = 30°$$

$$AF(\theta, \phi) = 2\left[\cos(X) - 2\cos\left(\frac{\sqrt{3}}{2}X\right)\cos\left(\frac{Y}{2}\right)\right.$$

$$\left. - \cos(Y) + 2\cos\left(\frac{X}{2}\right)\cos\left(\frac{\sqrt{3}}{2}Y\right)\right]$$

(15-9)

where

$$X = ks \sin\theta \cos\phi$$ (15-9a)

$$Y = ks \sin\theta \sin\phi$$ (15-9b)

These are assigned, at the end of the chapter, as exercises to the reader (Problem 15.2).

For a corner reflector with an included angle of $\alpha = 180°/n$, $n = 1, 2, 3, \ldots$, the number of images is equal to $N = (360/\alpha) - 1 = 2n - 1$.

It has also been shown [7] by using long filament wires as feeds, that the azimuthal plane ($\theta = \pi/2$) array factor for corner reflectors with $\alpha = 180°/n$, where n is an integer, can also be written as

$n = $ **even**   ($n = 2, 4, 6, \ldots$)

$$AF(\phi) = 4n(-1)^{n/2}[J_n(ks) \cos(n\phi) + J_{3n}(ks) \cos(3n\phi)$$

$$+ J_{5n}(ks) \cos(5n\phi) + \cdots]$$

(15-10a)

n = odd $(n = 1, 3, 5, ...)$

$$AF(\phi) = 4nj(-1)^{(n-1)/2}[J_n(ks) \cos(n\phi) - J_{3n}(ks) \cos(3n\phi)$$

$$+ J_{5n}(ks) \cos(5n\phi) + \cdots]$$ (15-10b)

where $J_m(x)$ is the Bessel function of the first kind of order m (see Appendix V).

When n is not an integer, the field must be found by retaining a sufficient number of terms of the infinite series. It has also been shown [7] that for all values of $n = m$ (integral or fractional) that the field can be written as

$$AF(\phi) = 4m[e^{jm\pi/2} J_m(ks) \cos(m\phi) + e^{j3m\pi/2} J_{3m}(ks) \cos(3m\phi) + \cdots]$$ (15-11)

The array factor for a corner reflector, as given by (15-10a)-(15-11), has a form that is similar to the array factor for a uniform circular array, as given by (6-121). This should be expected since the feed sources and their images in Figure 15.3 form a circular array. The number of images increase as the included angle of the corner reflector decreases.

Patterns have been computed for corner reflectors with included angles of 60°, 45°, and 30°. It has been found that these corner reflectors have also single-lobed patterns for the smaller values of s, and they become narrower as the included angle decreases. Multiple lobes begin to appear when

$$s \approx 0.95\lambda \quad \text{for} \quad \alpha = 60°$$

$$s \approx 1.2\lambda \quad \text{for} \quad \alpha = 45°$$

$$s \approx 2.5\lambda \quad \text{for} \quad \alpha = 30°$$

The field strength along the axis of symmetry ($\theta = 90°$, $\phi = 0°$) as a function of the feed-to-vertex distance s, has been computed for reflectors with included angles of $\alpha = 60°$, 45°, and 30°. The results for $\alpha = 45°$ are shown in Figure 15.7 for $0 \leq s \leq 10\lambda$.

For reflectors with $\alpha = 90°$ and 60°, the normalized field strength is periodic with periods of λ and 2λ, respectively. However, for the 45° and 30° reflectors the normalized field is not periodic but rather "almost periodic" or "pseudoperiodic" [8]. For the 45° and 30° reflectors the arguments of the trigonometric functions representing the arrays factors, and given by (15-8)-(15-9b), are related by irrational numbers and therefore the arrays factors do not repeat. However, when plotted they look very similar. Therefore when examined only graphically, the observer erroneously may conclude that the patterns are periodic (because they look so much the same). However, when the array factors are examined analytically it is concluded that the functions are not periodic but rather nearly periodic. The field variations are "nearly similar" in form in the range $\Delta s = 16.69\lambda$ for the $\alpha = 45°$ and $\Delta s = 30\lambda$ for the $\alpha = 30°$. Therefore the array factors of (15-8) and (15-9) belong to the class of *nearly periodic functions* [8].

It has also been found that the maximum field strength increases as the included angle of the reflector decreases. This is expected since a smaller angle reflector exhibits better directional characteristics because of the narrowness of its angle. The maximum values of $|E/E_0|$ for $\alpha = 60°$, 45°, and 30° are approximately 5.2, 8, and 9, respectively. The first field strength peak, but not necessarily the ultimate maximum, is achieved when

$$s \approx 0.65\lambda \quad \text{for} \quad \alpha = 60°$$

$$s \approx 0.85\lambda \quad \text{for} \quad \alpha = 45°$$
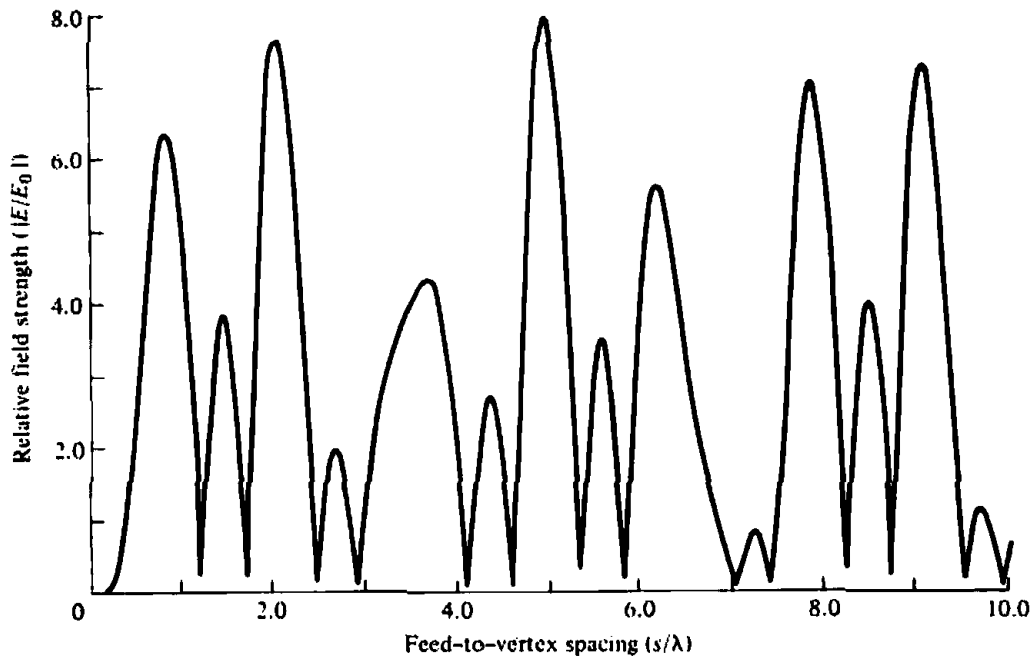
$$s \approx 1.20\lambda \quad \text{for} \quad \alpha = 30°$$

Figure 15.7   Relative field strength along the axis ($\theta = 90°$, $\phi = 0°$) for an $\alpha = 45°$ corner reflector as a function of feed-to-vertex spacing.

15.4 PARABOLIC REFLECTOR

The overall radiation characteristics (antenna pattern, antenna efficiency, polarization discrimination, etc.) of a reflector can be improved if the structural configuration of its surface is upgraded. It has been shown by geometrical optics that if a beam of parallel rays is incident upon a reflector whose geometrical shape is a parabola, the radiation will converge (focus) at a spot which is known as the *focal point*. In the same manner, if a point source is placed at the focal point, the rays reflected by a parabolic reflector will emerge as a parallel beam. This is one form of the principle of reciprocity, and it is demonstrated geometrically in Figure 15.1(c). The symmetrical point on the parabolic surface is known as the *vertex*. Rays that emerge in a parallel formation are usually said to be *collimated*. In practice, collimation is often used to describe the highly directional characteristics of an antenna even though the emanating rays are not exactly parallel. Since the transmitter (receiver) is placed at the focal point of the parabola, the configuration is usually known as *front fed*.

The disadvantage of the front-fed arrangement is that the transmission line from the feed must usually be long enough to reach the transmitting or the receiving equipment, which is usually placed behind or below the reflector. This may necessitate the use of long transmission lines whose losses may not be tolerable in many applications, especially in low-noise receiving systems. In some applications, the transmitting or receiving equipment is placed at the focal point to avoid the need for long transmission lines. However, in some of these applications, especially for transmission that may require large amplifiers and for low-noise receiving systems where cooling and weatherproofing may be necessary, the equipment may be too heavy and bulky and will provide undesirable blockage.

Another arrangement that avoids placing the feed (transmitter and/or receiver) at the focal point is that shown in Figure 15.1(d), and it is known as the *Cassegrain feed*. Through geometrical optics, Cassegrain, a famous astronomer (hence its name), showed that incident parallel rays can be focused to a point by utilizing two reflectors.

To accomplish this, the main (primary) reflector must be a parabola, the secondary reflector (subreflector) a hyperbola, and the feed placed along the axis of the parabola usually at or near the vertex. Cassegrain used this scheme to construct optical telescopes, and then its design was copied for use in radio frequency systems. For this arrangement, the rays that emanate from the feed illuminate the subreflector and are reflected by it in the direction of the primary reflector, as if they originated at the focal point of the parabola (primary reflector). The rays are then reflected by the primary reflector and are converted to parallel rays, provided the primary reflector is a parabola and the subreflector is a hyperbola. Diffractions occur at the edges of the subreflector and primary reflector, and they must be taken into account to accurately predict the overall system pattern, especially in regions of low intensity [9]–[11]. Even in regions of high intensity, diffractions must be included if an accurate formation of the fine ripple structure of the pattern is desired. With the Cassegrain-feed arrangement, the transmitting and/or receiving equipment can be placed behind the primary reflector. This scheme makes the system relatively more accessible for servicing and adjustments.

A parabolic reflector can take two different forms. One configuration is that of the parabolic right cylinder, shown in Figure 15.8(a), whose energy is collimated at a line that is parallel to the axis of the cylinder through the focal point of the reflector. The most widely used feed for this type of a reflector is a linear dipole, a linear array, or a slotted waveguide. The other reflector configuration is that of Figure 15.8(b) which is formed by rotating the parabola around its axis, and it is referred to as a *paraboloid* (parabola of revolution). A pyramidal or a conical horn has been widely utilized as a feed for this arrangement.

There are many other types of reflectors whose analysis is widely documented in the literature [12]–[14]. The spherical reflector, for example, has been utilized for radioastronomy and small earth station applications, because its beam can be efficiently scanned by moving its feed. An example of that is the 1,000-ft (305-m) diameter spherical reflector at Arecibo, Puerto Rico [12] whose primary surface is built into the ground and scanning of the beam is accomplished by movement of the feed. For spherical reflectors a substantial blockage may be provided by the feed leading to unacceptable minor lobe levels, in addition to the inherent reduction in gain and less favorable cross-polarization discrimination.

To eliminate some of the deficiencies of the symmetric configurations, offset-parabolic reflector designs have been developed for single- and dual-reflector systems
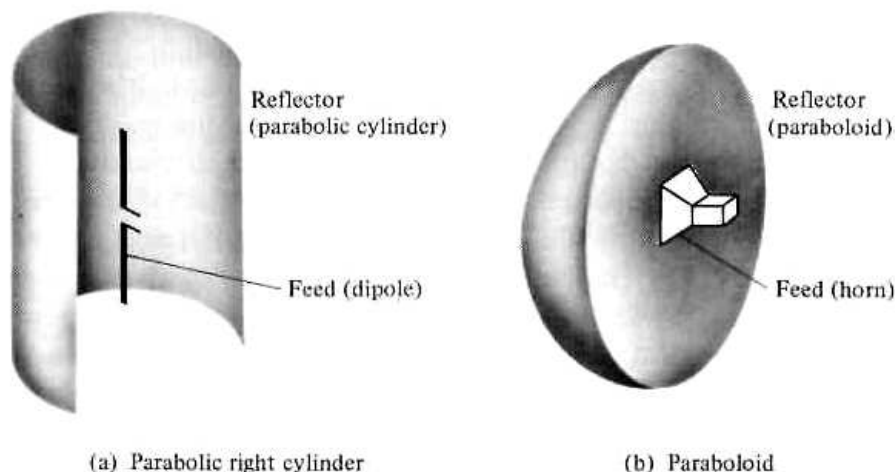

(a) Parabolic right cylinder   (b) Paraboloid

Figure 15.8 Parabolic right cylinder and paraboloid.

[13]. Because of the asymmetry of the system, the analysis is more complex. However the advent and advances of the computer technology have made the modeling and optimization of the offset reflector designs available and convenient. Offset reflector designs reduce aperture blocking and VSWR. In addition, they lead to the use of larger f/d ratios while maintaining acceptable structural rigidity, which provide an opportunity for improved feed-pattern shaping and better suppression of cross-polarized radiation emanating from the feed. However, offset-reflector configurations generate cross-polarized antenna radiation when illuminated by a linearly polarized primary-feed. Circularly polarized feeds eliminate depolarization, but they lead to squinting of the main beam from boresight. In addition, the structural asymmetry of the system is usually considered a major drawback.

Paraboloidal reflectors are the most widely used large aperture ground-based antennas [14]. At the time of its construction, the world's largest fully steerable reflector was the 100-m diameter radio telescope [15] of the Max Planck Institute for Radioastronomy at Effelsberg, West Germany, while the largest in the United States was the 64-m diameter [16] reflector at Goldstone, California built primarily for deep-space applications. When fed efficiently from the focal point, paraboloidal reflectors produce a high gain pencil beam with low side lobes and good cross-polarization discrimination characteristics. This type of an antenna is widely used for low-noise applications, such as in radioastronomy, and it is considered as a good compromise between performance and cost. To build a large reflector requires not only a large financial budget but also a difficult structural undertaking, because it must withstand severe weather conditions.

Cassegrain designs, employing dual reflector surfaces, are used in applications where pattern control is essential, such as in satellite ground-based systems, and have efficiencies of 65–80%. They supersede the performance of the single-reflector front-fed arrangement by about 10%. Using geometrical optics, the classical Cassegrain configuration, consisting of a paraboloid and a hyperboloid, is designed to achieve a uniform phase front in the aperture of the paraboloid. By employing good feed designs, this arrangement can achieve lower spillover and more uniform illumination of the main reflector. In addition, slight shaping of one or both of the dual-reflector's surfaces can lead to an aperture with almost uniform amplitude and phase with a substantial enhancement in gain [14]. These are referred to as *shaped* reflectors. Shaping techniques have been employed in dual-reflectors used in earth station applications. An example is the 10-m earth station dual-reflector antenna, shown in Figure 15.9, whose *main reflector and subreflector are shaped.*

For many years horns or waveguides, operating in a single mode, were used as feeds for reflector antennas. However because of radioastronomy and earth-station applications, considerable efforts have been placed in designing more efficient feeds to illuminate either the main reflector or the subreflector. It has been found that corrugated horns that support hybrid mode fields (combination of TE and TM modes) can be used as desirable feeds. Such feed elements match efficiently the fields of the feeds with the desired focal distribution produced by the reflector, and they can reduce cross-polarization. Dielectric cylinders and cones are other antenna structures that support hybrid modes [14]. Their structural configuration can also be used to support the subreflector and to provide attractive performance figures.

There are primarily two techniques that can be used to analyze the performance of a reflector system [17]. One technique is the *aperture distribution method* and the other the *current distribution method.* Both techniques will be introduced to show the similarities and differences.

Figure 15.9 Shaped 10-m earth station dual-reflector antenna (courtesy Andrew Corp.).

15.4.1 Front-Fed Parabolic Reflector

Parabolic cylinders have widely been used as high-gain apertures fed by line sources. The analysis of a parabolic cylinder (single curved) reflector is similar, but considerably simpler than that of a paraboloidal (double curved) reflector. The principal characteristics of aperture amplitude, phase, and polarization for a parabolic cylinder, as contrasted to those of a paraboloid, are as follows:

1. The amplitude taper, due to variations in distance from the feed to the surface of the reflector, is proportional to $1/\rho$ in a cylinder compared to $1/r^2$ in a paraboloid.

2. The focal region, where incident plane waves converge, is a line-source for a cylinder and a point source for a paraboloid.

3. When the fields of the feed are linearly polarized parallel to the axis of the cylinder, no cross-polarized components are produced by the parabolic cylinder. That is not the case for a paraboloid.

Generally, parabolic cylinders, as compared to paraboloids, (1) are mechanically simpler to build, (2) provide larger aperture blockage, and (3) do not possess the attractive characteristics of a paraboloid. In this chapter, only paraboloidal reflectors will be examined.

A. Surface Geometry

The surface of a paraboloidal reflector is formed by rotating a parabola about its axis. Its surface must be a paraboloid of revolution so that rays emanating from the focus of the reflector are transformed into plane waves. The design is based on optical techniques, and it does not take into account any deformations (diffractions) from the rim of the reflector. Referring to Figure 15.10 and choosing a plane perpendicular to the axis of the reflector through the focus, it follows that

$$OP + PQ = \text{constant} = 2f \tag{15-12}$$

Since

$$OP = r' \tag{15-13}$$

$$PQ = r' \cos \theta'$$

(15-12) can be written as

$$r'(1 + \cos \theta') = 2f \tag{15-14}$$

or

$$r' = \frac{2f}{1 + \cos \theta'} = f \sec^2\left(\frac{\theta'}{2}\right) \qquad \theta \le \theta_0 \tag{15-14a}$$
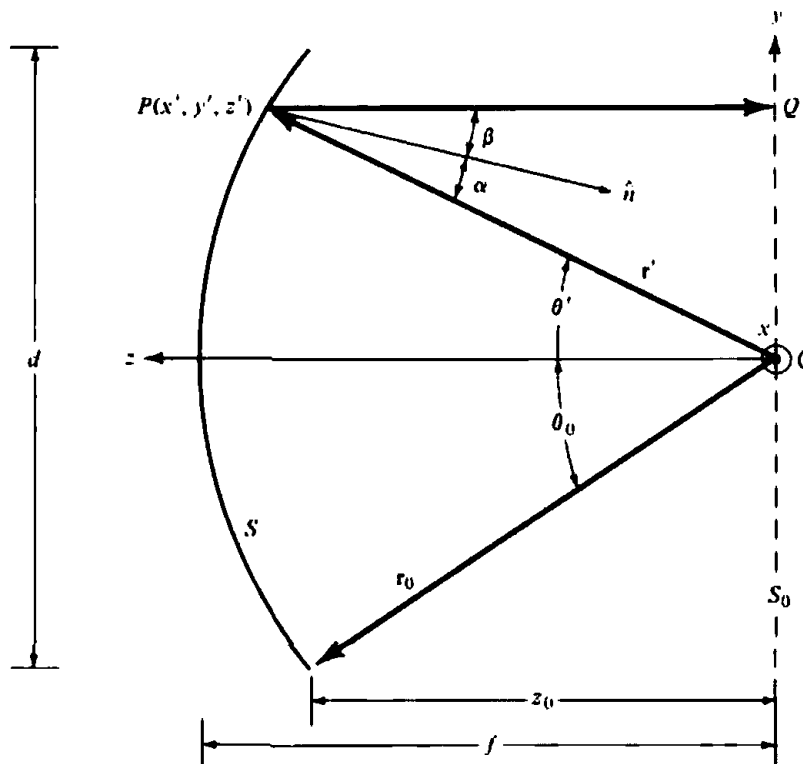

Figure 15.10 Two-dimensional configuration of a paraboloidal reflector.

Since a paraboloid is a parabola of revolution (about its axis), (15-14a) is also the equation of a paraboloid in terms of the spherical coordinates r', θ', ϕ'. Because of its rotational symmetry, there are no variations with respect to ϕ'.

Equation (15-14a) can also be written in terms of the rectangular coordinates x', y', z'. That is,

$$r' + r' \cos \theta' = \sqrt{(x')^2 + (y')^2 + (z')^2} + z' = 2f \qquad (15\text{-}15)$$

or

$$(x')^2 + (y')^2 = 4f(f - z') \qquad \text{with } (x')^2 + (y')^2 \leq (d/2)^2 \qquad (15\text{-}15a)$$

In the analysis of parabolic reflectors, it is desirable to find a unit vector that is normal to the local tangent at the surface reflection point. To do this, (15-14a) is first expressed as

$$f - r' \cos^2\left(\frac{\theta'}{2}\right) = S = 0 \qquad (15\text{-}16)$$

and then a gradient is taken to form a normal to the surface. That is,

$$N = \nabla\left[f - r' \cos^2\left(\frac{\theta'}{2}\right)\right] = \hat{a}_{r'} \frac{\partial S}{\partial r'} + \hat{a}_{\theta'} \frac{1}{r'} \frac{\partial S}{\partial \theta'}$$

$$= -\hat{a}_{r'} \cos^2\left(\frac{\theta'}{2}\right) + \hat{a}_{\theta'} \cos\left(\frac{\theta'}{2}\right) \sin\left(\frac{\theta'}{2}\right) \qquad (15\text{-}17)$$

A unit vector, normal to S, is formed from (15-17) as

$$\hat{n} = \frac{N}{|N|} = -\hat{a}_{r'} \cos\left(\frac{\theta'}{2}\right) + \hat{a}_{\theta'} \sin\left(\frac{\theta'}{2}\right) \qquad (15\text{-}18)$$

To find the angle between the unit vector $\hat{n}$ which is normal to the surface at the reflection point, and a vector directed from the focus to the reflection point, we form

$$\cos \alpha = -\hat{a}_{r'} \cdot \hat{n} = -\hat{a}_{r'} \cdot \left[-\hat{a}_{r'} \cos\left(\frac{\theta'}{2}\right) + \hat{a}_{\theta'} \sin\left(\frac{\theta'}{2}\right)\right]$$

$$= \cos\left(\frac{\theta'}{2}\right) \qquad (15\text{-}19)$$

In a similar manner we can find the angle between the unit vector $\hat{n}$ and the z-axis. That is,

$$\cos \beta = -\hat{a}_z \cdot \hat{n} = -\hat{a}_z \cdot \left[-\hat{a}_{r'} \cos\left(\frac{\theta'}{2}\right) + \hat{a}_{\theta'} \sin\left(\frac{\theta'}{2}\right)\right] \qquad (15\text{-}20)$$

Using the transformation of (4-5), (15-20) can be written as

$$\cos \beta = -(\hat{a}_{r'} \cos \theta' - \hat{a}_{\theta'} \sin \theta') \cdot \left[-\hat{a}_{r'} \cos\left(\frac{\theta'}{2}\right) + \hat{a}_{\theta'} \sin\left(\frac{\theta'}{2}\right)\right]$$

$$= \cos\left(\frac{\theta'}{2}\right) \qquad (15\text{-}21)$$

which is identical to α of (15-19). This is nothing more than a verification of Snell's law of reflection at each differential area of the surface, which has been assumed to be flat locally.

Another expression that is usually very prominent in the analysis of reflectors is that relating the subtended angle θ_0 to the f/d ratio. From the geometry of Figure 15.10

$$\theta_0 = \tan^{-1}\left(\frac{d/2}{z_0}\right) \tag{15-22}$$

where z_0 is the distance along the axis of the reflector from the focal point to the edge of the rim. From (15-15a)

$$z_0 = f - \frac{x_0^2 + y_0^2}{4f} = f - \frac{(d/2)^2}{4f} = f - \frac{d^2}{16f} \tag{15-23}$$

Substituting (15-23) into (15-22) reduces it to

$$\theta_0 = \tan^{-1}\left|\frac{\dfrac{d}{2}}{f - \dfrac{d^2}{16f}}\right| = \tan^{-1}\left|\frac{\dfrac{1}{2}\left(\dfrac{f}{d}\right)}{\left(\dfrac{f}{d}\right)^2 - \dfrac{1}{16}}\right| \tag{15-24}$$

It can also be shown that another form of (15-24) is

$$f = \left(\frac{d}{4}\right)\cot\left(\frac{\theta_0}{2}\right) \tag{15-25}$$

B. Induced Current Density

To determine the radiation characteristics (pattern, gain, efficiency, polarization, etc.) of a parabolic reflector, the current density induced on its surface must be known. The current density $\mathbf{J}_s$ can be determined by using

$$\mathbf{J}_s = \hat{n} \times \mathbf{H} = \hat{n} \times (\mathbf{H}^i + \mathbf{H}^r) \tag{15-26}$$

where $\mathbf{H}^i$ and $\mathbf{H}^r$ represent, respectively, the incident and reflected magnetic field components evaluated at the surface of the conductor, and $\hat{n}$ is a unit vector normal to the surface. If the reflecting surface can be approximated by an *infinite plane surface* (this condition is met locally for a parabola), then by the method of images

$$\hat{n} \times \mathbf{H}^i = \hat{n} \times \mathbf{H}^r \tag{15-27}$$

and (15-26) reduces to

$$\mathbf{J}_s = \hat{n} \times (\mathbf{H}^i + \mathbf{H}^r) = 2\hat{n} \times \mathbf{H}^i = 2\hat{n} \times \mathbf{H}^r \tag{15-28}$$

The current density approximation of (15-28) is known as the *physical-optics* approximation, and it is valid when the transverse dimensions of the reflector, radius of curvature of the reflecting object, and the radius of curvature of the incident wave are large compared to a wavelength.

If the reflecting surface is in the far-field of the source generating the incident waves, then (15-28) can also be written as

$$\mathbf{J}_s = 2\hat{n} \times \mathbf{H}^i \simeq \frac{2}{\eta}[\hat{n} \times (\hat{s}_i \times \mathbf{E}^i)] \qquad (15\text{-}29)$$

or

$$\mathbf{J}_s = 2\hat{n} \times \mathbf{H}^r \simeq \frac{2}{\eta}[\hat{n} \times (\hat{s}_r \times \mathbf{E}^r)] \qquad (15\text{-}29a)$$

where η is the intrinsic impedance of the medium, $\hat{s}_i$ and $\hat{s}_r$ are radial unit vectors along the ray paths of the incident and reflected waves (as shown in Figure 15.11), and $\mathbf{E}^i$ and $\mathbf{E}^r$ are the incident and reflected electric fields.

C. Aperture Distribution Method

It was pointed out earlier that the two most commonly used techniques in analyzing the radiation characteristics of reflectors are the *aperture distribution* and the *current distribution* methods.

For the aperture distribution method, the field reflected by the surface of the paraboloid is first found over a plane which is normal to the axis of the reflector. Geometrical optics techniques (ray tracing) are usually employed to accomplish this. In most cases, the plane is taken through the focal point, and it is designated as the *aperture plane*, as shown in Figure 15.12. Equivalent sources are then formed over that plane. Usually it is assumed that the equivalent sources are zero outside the projected area of the reflector on the aperture plane. These equivalent sources are then used to compute the radiated fields utilizing the aperture techniques of Chapter 12.

For the *current distribution method*, the physical optics approximation of the induced current density $\mathbf{J}_s$ given by (15-28) ($\mathbf{J}_s \simeq 2\hat{n} \times \mathbf{H}^i$ where $\mathbf{H}^i$ is the incident magnetic field and $\hat{n}$ is a unit vector normal to the reflector surface) is formulated over the illuminated side of the reflector (S_1) of Figure 15.11. This current density is then integrated over the surface of the reflector to yield the far-zone radiation fields.

For the reflector of Figure 15.11, approximations that are common to both methods are:

1. The current density is zero on the shadow side (S_2) of the reflector.
2. The discontinuity of the current density over the rim (Γ) of the reflector is neglected.
3. Direct radiation from the feed and aperture blockage by the feed are neglected.
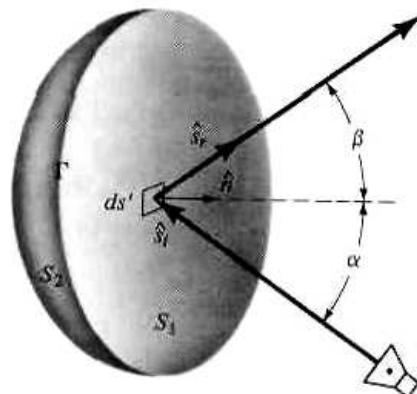

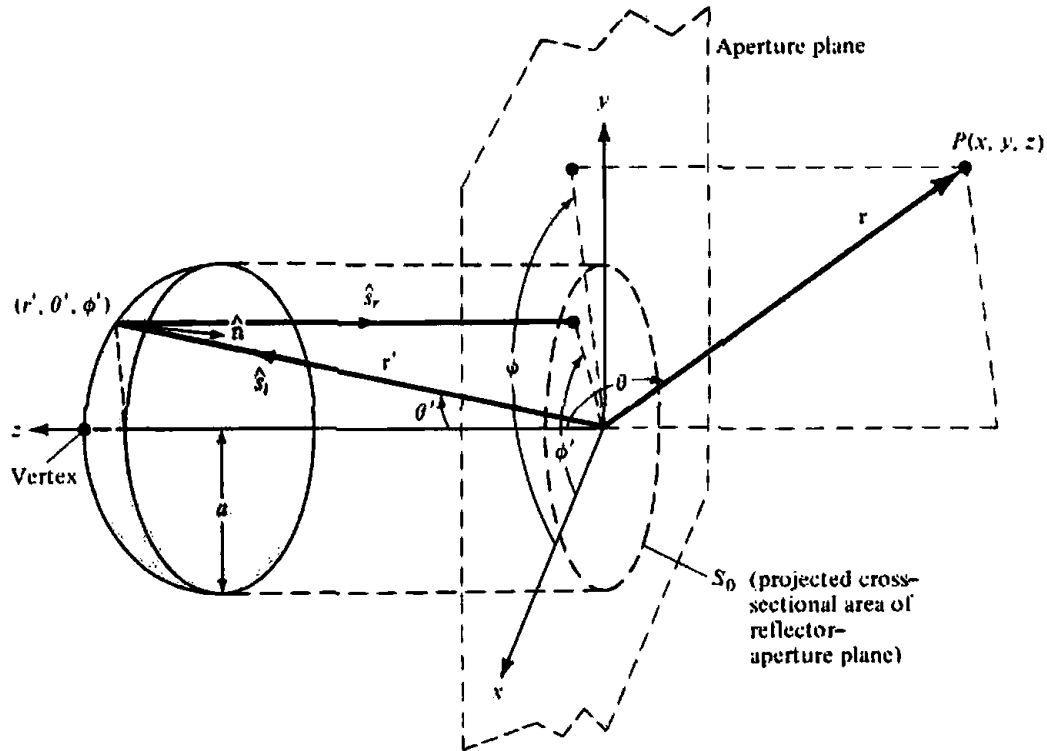**Figure 15.11**   Reflecting surface with boundary Γ.

Figure 15.12 Three-dimensional geometry of a paraboloidal reflector system.

These approximations lead to accurate results, using either technique, for the radiated fields on the main beam and nearby minor lobes. To predict the pattern more accurately in all regions, especially the far minor lobes, geometrical diffraction techniques [9]–[11] can be applied. Because of the level of the material, it will not be included here. The interested reader can refer to the literature.

The advantage of the aperture distribution method is that the integration over the aperture plane can be performed with equal ease for any feed pattern or feed position [18]. The integration over the surface of the reflector as required for the current distribution method, becomes quite complex and time consuming when the feed pattern is asymmetrical and/or the feed is placed off-axis.

Let us assume that a y-polarized source with a gain function of $G_f(\theta', \phi')$ is placed at the focal point of a paraboloidal reflector. The radiation intensity of this source is given by

$$U(\theta', \phi') = \frac{P_t}{4\pi} G_f(\theta', \phi') \qquad (15\text{-}30)$$

where P_t is the total radiated power. Referring to Figure 15.12, at a point r' in the far-zone of the source

$$U(\theta', \phi') = \frac{1}{2} \text{Re}[\mathbf{E}^\circ(\theta', \phi') \times \mathbf{H}^{\circ*}(\theta', \phi')] = \frac{1}{2\eta} |\mathbf{E}^\circ(\theta', \phi')|^2 \qquad (15\text{-}31)$$

or

$$|\mathbf{E}^\circ(\theta', \phi')| = [2\eta \, U(\theta', \phi')]^{1/2} = \left[\eta \frac{P_t}{2\pi} G_f(\theta', \phi') \right]^{1/2} \qquad (15\text{-}31a)$$

The incident field, with a direction perpendicular to the radial distance, can then be written as

$$E^i(r', \theta', \phi') = \hat{e}_i \left[\sqrt{\frac{\mu}{\epsilon} \frac{P_t}{2\pi}} \, G_f(\theta', \phi') \right]^{1/2} \frac{e^{-jkr'}}{r'} = \hat{e}_i C_1 \sqrt{G_f(\theta', \phi')} \, \frac{e^{-jkr'}}{r'}$$

(15-32)

$$C_1 = \left(\frac{\mu}{\epsilon}\right)^{1/4} \left(\frac{P_t}{2\pi}\right)^{1/2}$$

(15-32a)

where $\hat{e}_i$ is a unit vector perpendicular to $\hat{a}_r'$ and parallel to the plane formed by $\hat{a}_r'$ and $\hat{a}_y$, as shown in Figure 15.13.

It can be shown [19] that on the surface of the reflector

$$J_s = 2 \sqrt{\frac{\epsilon}{\mu}} [\hat{n} \times (\hat{s}_i \times E^i)] = 2 \sqrt{\frac{\epsilon}{\mu}} C_1 \sqrt{G_f(\theta', \phi')} \, \frac{e^{-jkr'}}{r'} \mathbf{u}$$

(15-33)

where

$$\mathbf{u} = \hat{n} \times (\hat{a}_r' \times \hat{e}_i) = (\hat{n} \cdot \hat{e}_i)\hat{a}_r' - (\hat{n} \cdot \hat{a}_r')\hat{e}_i$$

(15-33a)

which reduces to

$$\mathbf{u} = \left[- \hat{a}_x \sin \theta' \sin \left(\frac{\theta'}{2}\right) \sin \phi' \cos \phi' \right.$$

$$+ \hat{a}_y \cos \left(\frac{\theta'}{2}\right) (\sin^2 \phi' \cos \theta' + \cos^2 \phi')$$

$$\left. - \hat{a}_z \cos \theta' \sin \phi' \sin \left(\frac{\theta'}{2}\right) \right] \Big/ \sqrt{1 - \sin^2 \theta' \sin^2 \phi'}$$

(15-34)

To find the aperture field E_{ap} at the plane through the focal point, due to the reflector currents of (15-33), the reflected field E^r at r' (the reflection point) is first found. This is of the form

$$E^r = \hat{e}_r C_1 \sqrt{G_f(\theta', \phi')} \, \frac{e^{-jkr'}}{r'}$$

(15-35)

where $\hat{e}_r$ is a unit vector depicting the polarization of the reflected field. From (15-29a)

$$J_s = 2 \sqrt{\frac{\epsilon}{\mu}} [\hat{n} \times (\hat{s}_r \times E^r)]$$

(15-36)

Because $\hat{s}_r = -\hat{a}_z$, (15-36) can be written, using (15-35), as

$$J_s = 2 \sqrt{\frac{\epsilon}{\mu}} C_1 \sqrt{G_f(\theta', \phi')} \, \frac{e^{-jkr'}}{r'} \mathbf{u}$$

(15-37)

where

$$\mathbf{u} = \hat{n} \times (- \hat{a}_z \times \hat{e}_r) = -\hat{a}_z(\hat{n} \cdot \hat{e}_r) - \hat{e}_r \cos \left(\frac{\theta'}{2}\right)$$
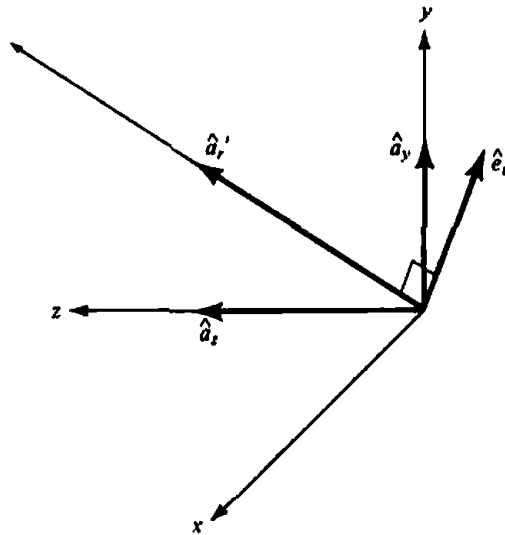
(15-37a)

Figure 15.13   Unit vector alignment for a paraboloidal reflector system.

Since **u** in (15-37) and (15-37a) is the same as that of (15-33)–(15-34), it can be shown [19] through some extensive mathematical manipulations that

$$\hat{e}_r = \frac{\hat{a}_x \sin \phi' \cos \phi' (1 - \cos \theta') - \hat{a}_y (\sin^2 \phi' \cos \theta' + \cos^2 \phi')}{\sqrt{1 - \sin^2 \theta' \sin^2 \phi'}}$$

(15-38)

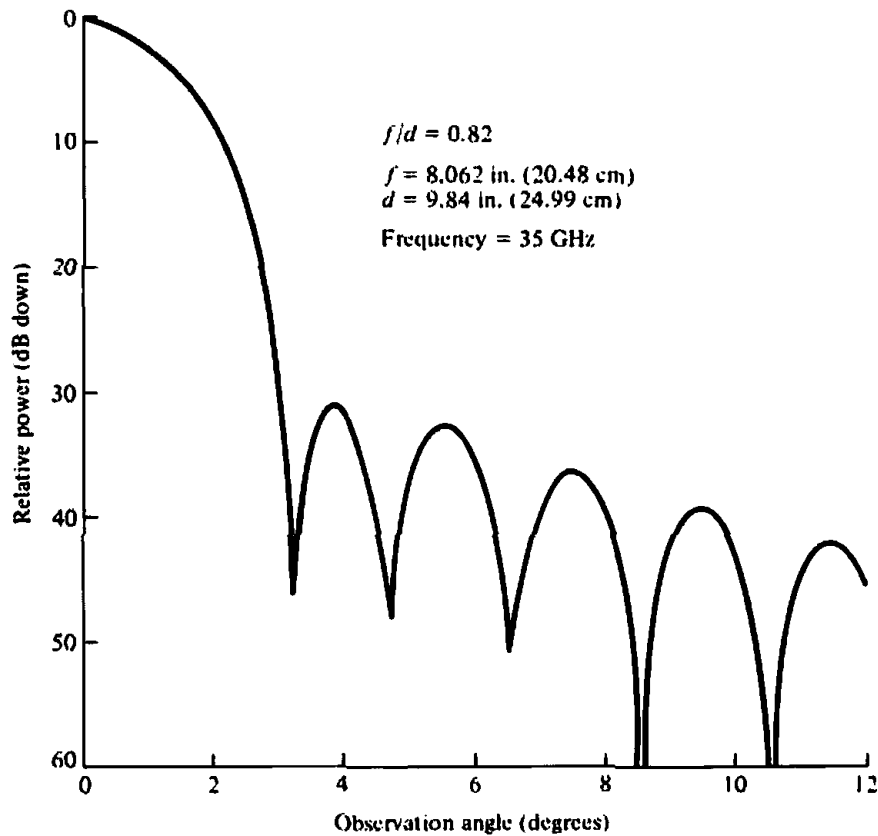$f/d = 0.82$

$f = 8.062$ in. (20.48 cm)
$d = 9.84$ in. (24.99 cm)

Frequency = 35 GHz

Figure 15.14   Principal E- or H-plane pattern of a symmetrical front-fed paraboloidal reflector (courtesy M. C. Bailey, NASA Langley Research Center).

Thus the field E^r at the point of reflection r' is given by (15-35) where $\hat{e}_r$ is given by (15-38). At the plane passing through the focal point, the field is given by

$$\mathbf{E}_{np} = \hat{e}_r C_1 \sqrt{G_f(\theta', \phi')} \frac{e^{-jkr'(1+\cos\theta')}}{r'} = \hat{a}_x E_{xa} + \hat{a}_y E_{ya} \qquad (15-39)$$

where E_{xa} and E_{ya} represent the x- and y-components of the reflected field over the aperture. Since the field from the reflector to the aperture plane is a plane wave, no correction in amplitude is needed to account for amplitude spreading.

Using the reflected electric field components (E_{xa} and E_{ya}) as given by (15-39), an equivalent is formed at the aperture plane. That is,

$$\mathbf{J}'_s = \hat{n} \times \mathbf{H}_a = -\hat{a}_z \times \left(\hat{a}_x \frac{E_{ay}}{\eta} - \hat{a}_y \frac{E_{ax}}{\eta}\right) = -\hat{a}_x \frac{E_{ax}}{\eta} - \hat{a}_y \frac{E_{ay}}{\eta} \qquad (15\text{-}40a)$$

$$\mathbf{M}'_s = -\hat{n} \times \mathbf{E}_a = +\hat{a}_z \times (\hat{a}_x E_{ax} + \hat{a}_y E_{ay}) = -\hat{a}_x E_{ay} + \hat{a}_y E_{ax} \qquad (15\text{-}40b)$$

The radiated field can be computed using the (15-40a), (15-40b), and the formulations of Section 12.3. The integration is restricted only over the projected cross-sectional area S_0 of the reflector at the aperture plane shown dashed in Figure 15.12. That is,

$$E_{\theta s} = \frac{jke^{-jkr}}{4\pi r}(1 - \cos\theta) \iint_{S_0} (-E_{ax}\cos\phi - E_{ay}\sin\phi)$$
$$\times e^{jk(x'\sin\theta\cos\phi + y'\sin\theta\sin\phi)} dx' dy' \qquad (15\text{-}41a)$$

$$E_{\phi s} = \frac{jke^{-jkr}}{4\pi r}(1 - \cos\theta) \iint_{S_0} (-E_{ax}\sin\phi + E_{ay}\cos\phi)$$
$$\times e^{jk(x'\sin\theta\cos\phi + y'\sin\theta\sin\phi)} dx' dy' \qquad (15\text{-}41b)$$

The aperture distribution method has been used to compute, using efficient numerical integration techniques, the radiation patterns of paraboloidal [18] and spherical [20] reflectors. The fields given by (15-41a) and (15-41b) represent only the secondary pattern due to scattering from the reflector. The total pattern of the system is represented by the sum of secondary pattern and the primary pattern of the feed element. For most feeds (such as horns), the primary pattern in the boresight (forward) direction of the reflector is of very low intensity and usually can be neglected.

To demonstrate the utility of the techniques, the principal E- and H-plane secondary patterns of a 35 GHz reflector, with an $f/d = 0.82$ [$f = 8.062$ in. (20.48 cm), $d = 9.84$ in. (24.99 cm)] and fed by a conical dual-mode horn, were computed and they are displayed in Figure 15.14. Since the feed horn has identical E- and H-plane patterns and the reflector is fed symmetrically, the reflector E- and H-plane patterns are also identical and do not possess any cross-polarized components.

To simultaneously display the field intensity associated with each point in the aperture plane of the reflector, a computer generated plot was developed [20]. The field point locations, showing quantized contours of constant amplitude in the aperture plane, are illustrated in Figure 15.15. The reflector system has an $f/d = 0.82$ with the same physical dimensions [$f = 8.062$ in. (20.48 cm), $d = 9.84$ in. (24.99 cm)] and the same feed as the principal pattern of Figure 15.14. One symbol is used to represent the amplitude level of each 3-dB region. The field intensity within the bounds of the reflector aperture plane is within the 0–15 dB range.
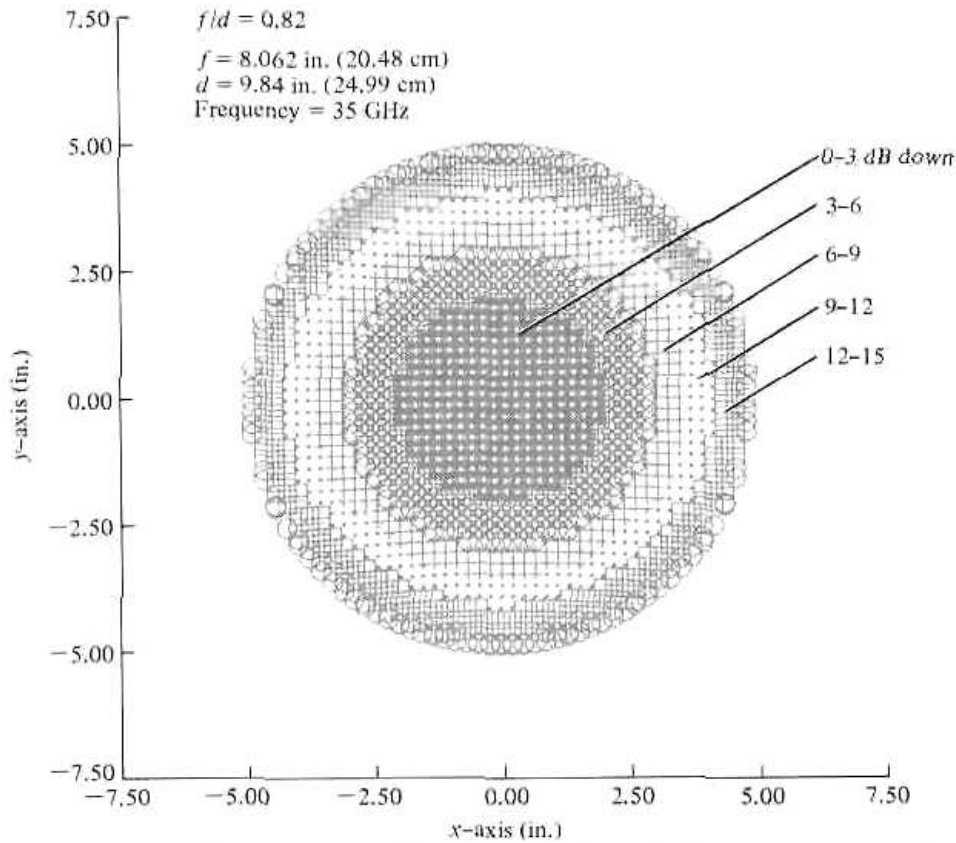
Figure 15.15 Field point locations of constant amplitude contours in the aperture plane of a symmetrical front-fed paraboloidal reflector (courtesy M. C. Bailey, NASA Langley Research Center).

D. Cross-Polarization

The field reflected by the paraboloid, as represented by (15-35) and (15-38) of the aperture distribution method, contains x- and y-polarized components when the incident field is y-polarized. The y-component is designated as the *principal polarization* and the x-component as the *cross-polarization*. This is illustrated in Figure 15.16. It is also evident that symmetrical (with respect to the principal planes) cross-polarized components are $180°$ out of phase with one another. However for very narrow beam reflectors or for angles near the boresight axis ($\theta' \simeq 0°$), the cross-polarized x-component diminishes and it vanishes on axis ($\theta' = 0°$). A similar procedure can be used to show that for an incident x-polarized field, the reflecting surface decomposes the wave to a y-polarized field, in addition to its x-polarized component.

An interesting observation about the polarization phenomenon of a parabolic reflector can be made if we first assume that the feed element is an infinitesimal electric dipole ($l \ll \lambda$) with its length along the y-axis. For that feed, the field reflected by the reflector is given by (15-35) where from (4-114)

$$C_1\sqrt{G_f(\theta', \phi')} = j\eta\frac{kI_0l}{4\pi}\sin\psi = j\eta\frac{kI_0l}{4\pi}\sqrt{1 - \cos^2\psi}$$

$$= j\eta\frac{kI_0l}{4\pi}\sqrt{1 - \sin^2\theta'\sin^2\phi'} \qquad (15\text{-}42)$$

The angle ψ is measured from the y-axis toward the observation point.
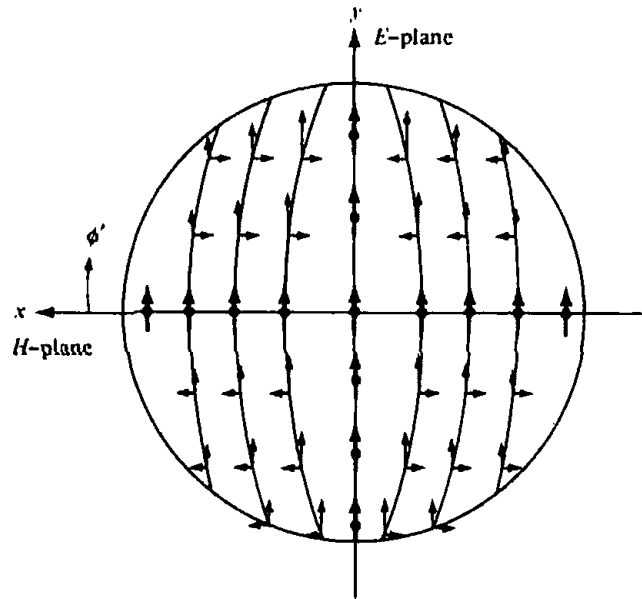
Figure 15.16 Principal (y-direction) and cross-polarization (x-direction) components of a paraboloidal reflector. (SOURCE: S. Silver (ed.). *Microwave Antenna Theory and Design* (MIT Radiation Lab. Series, Vol. 12). McGraw-Hill, New York, 1949)

When (15-42) is inserted in (15-35), we can write with the aid of (15-38) that

$$\mathbf{E}^r = [\hat{a}_x \sin \phi' \cos \phi'(1 - \cos \theta') - \hat{a}_y(\sin^2 \phi' \cos\theta' + \cos^2 \phi')]$$

$$\times j\eta \frac{kI_0 l}{4\pi} \frac{e^{-jkr'}}{r'} \tag{15-43}$$

Now let us assume that an infinitesimal magnetic dipole, with its length along the x-axis (or a small loop with its area parallel to the y-z plane) and with a magnetic moment of $-\hat{a}_x M$, is placed at the focal point and used as a feed. It can be shown [21]-[23] that the field reflected by the reflector has x- and y-components. However the x-component has a reverse sign to the x-component of the electric dipole feed. By adjusting the ratio of the electric to the magnetic dipole moments to be equal to $\sqrt{\mu/\epsilon}$, the two cross-polarized reflected components (x-components) can be made equal in magnitude and for their sum to vanish (because of reverse signs). Thus a cross electric and magnetic dipole combination located at the focal point of a paraboloid can be used to induce currents on the surface of the reflector which are parallel everywhere. This is illustrated graphically in Figure 15.17.

The direction of the induced current flow determines the far-field polarization of the antenna. Thus for the crossed electric and magnetic dipole combination feed, the far-field radiation is free of cross-polarization. This type of feed is "ideal" in that it does not require that the surface of the reflector be solid but can be formed by closely spaced parallel conductors. Because of its ideal characteristics. it is usually referred to as a *Huygens' source*.

E. Current Distribution Method

The current distribution method was introduced as a technique that can be used to better approximate. as compared to the geometrical-optics (ray-tracing) method. the field scattered from a surface. Usually the main difficulty in applying this method is the approximation of the current density over the surface of the scatterer.
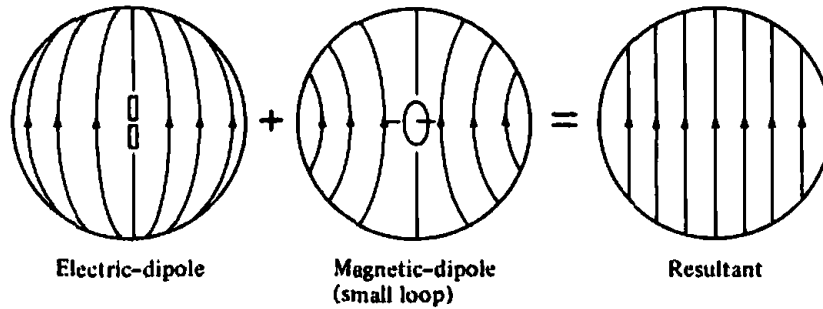
Electric-dipole   Magnetic-dipole   Resultant
                   (small loop)

Figure 15.17 Electric and magnetic dipole fields combined to form a Huygens' source with ideal feed polarization for reflector. (SOURCE: A. W. Love. "Some Highlights in Reflector Antenna Development," *Radio Science*, Vol. 11, Nos. 8, 9, August–September 1976)

To analyze the reflector using this technique, we refer to the radiation integrals and auxiliary potential functions formulations of Chapter 3. While the two-step procedure of Figure 3.1 often simplifies the solution of most problems, the one-step formulation of Figure 3.1 is most convenient for the reflectors.

Using the potential function methods outlined in Chapter 3, and referring to the coordinate system of Figure 12.2(a), it can be shown [17] that the E- and H-fields radiated by the sources **J** and **M** can be written as

$$E = E_A + E_F = -j\frac{1}{4\pi\omega\epsilon}\int_V [(J \cdot \nabla)\nabla + k^2 J + j\omega\epsilon M \times \nabla]\frac{e^{-jkR}}{R}dv'$$

(15-44a)

$$H = H_A + H_F = -j\frac{1}{4\pi\omega\mu}\int_V [(M \cdot \nabla)\nabla + k^2 M - j\omega\mu J \times \nabla]\frac{e^{-jkR}}{R}dv'$$

(15-44b)

which for far-field observations reduce, according to the coordinate system of Figure 12.2(b), to

$$E = -j\frac{\omega\mu}{4\pi r}e^{-jkr}\int_{V'}\left[J - (J \cdot \hat{a}_r)\hat{a}_r + \sqrt{\frac{\epsilon}{\mu}}M \times \hat{a}_r\right]e^{+jkr'\cdot\hat{a}_r}dv'$$ (15-45a)

$$H = -j\frac{\omega\epsilon}{4\pi r}e^{-jkr}\int_V\left[M - (M \cdot \hat{a}_r)\hat{a}_r - \sqrt{\frac{\mu}{\epsilon}}J \times \hat{a}_r\right]e^{+jkr'\cdot\hat{a}_r}dv'$$ (15-45b)

If the current distributions are induced by electric and magnetic fields incident on a perfect electric conducting ($\sigma = \infty$) surface shown in Figure 15.18, the fields created by these currents are referred to as *scattered fields*. If the conducting surface is closed, the far-zone fields are obtained from (15-45a) and (15-45b) by letting **M** = 0 and reducing the volume integral to a surface integral with the surface current density **J** replaced by the linear current density **J**$_s$. Thus

$$E_s = -j\frac{\omega\mu}{4\pi r}e^{-jkr}\oint_S [J_s - (J_s \cdot \hat{a}_r)\hat{a}_r]e^{+jkr'\cdot\hat{a}_r}ds'$$

(15-46a)

$$H_s = +j\frac{\omega\sqrt{\mu\epsilon}}{4\pi r}e^{-jkr}\oint_S [J_s \times \hat{a}_r]e^{+jkr'\cdot\hat{a}_r}ds'$$
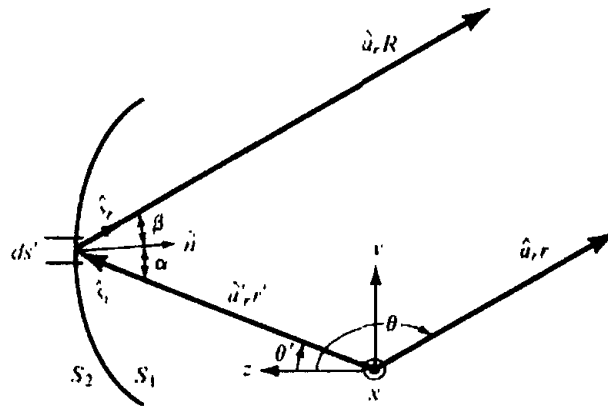
(15-46b)

Figure 15.18 Geometrical arrangement of reflecting surface.

The electric and magnetic fields scattered by the closed surface of the reflector of Figure 15.11, and given by (15-46a) and (15-46b), are valid provided the source-density functions (current and charge) satisfy the equation of continuity. This would be satisfied if the scattering object is a smooth closed surface. For the geometry of Figure 15.11, the current distribution is discontinuous across the boundary Γ (being zero over the shadow area S_2) which divides the illuminated (S_1) and shadow (S_2) areas. It can be shown [17] that the equation of continuity can be satisfied if an appropriate line source distribution of charge is introduced along the boundary Γ. Therefore the total scattered field would be the sum of the (1) surface currents over the illuminated area, (2) surface charges over the illuminated area, and (3) line charge distribution over the boundary Γ.

The contributions from the surface charge density are taken into account by the current distribution through the equation of continuity. However it can be shown [17] that in the far-zone the contribution due to line-charge distribution cancels out the longitudinal component introduced by the surface current and charge distributions. Since in the far-zone the field components are predominantly transverse, the contribution due to the line-charge distribution need not be included and (15-46a)–(15-46b) can be applied to an open surface.

In this section, (15-46a) and (15-46b) will be used to calculate the field scattered from the surface of a parabolic reflector. Generally the field radiated by the currents on the shadow region of the reflector is very small compared to the total field, and the currents and field can be set equal to zero. The field scattered by the illuminated (concave) side of the parabolic reflector can be formulated, using the current distribution method, by (15-46a) and (15-46b) when the integration is restricted over the illuminated area.

The total field of the system can be obtained by a superposition of the radiation from the primary source in directions greater than θ_0 ($\theta > \theta_0$) and that scattered by the surface as obtained by using either the aperture distribution or the current distribution method.

Generally edge effects are neglected. However the inclusion of diffracted fields [9]–[11] from the rim of the reflector not only introduce fields in the shadow region of the reflector, but also modify those present in the transition and lit regions. Any discontinuities introduced by geometrical optics methods along the transition region (between lit and shadow regions) are removed by the diffracted components.

The far-zone electric field of a parabolic reflector, neglecting the direct radiation, is given by (15-46a). When expanded, (15-46a) reduces, by referring to the geometry of Figure 15.18, to the two components of
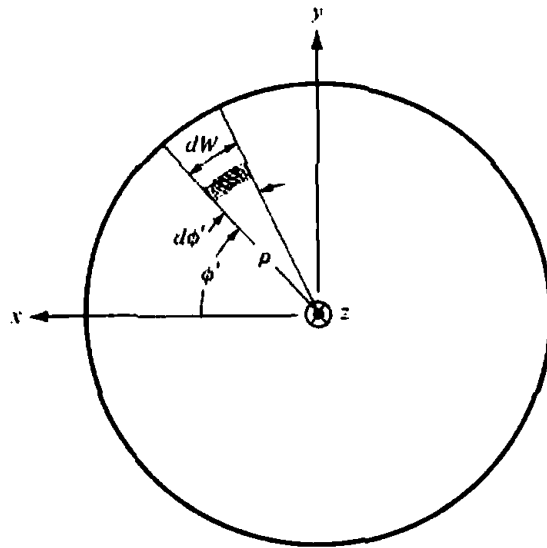
(a) Projected cross section
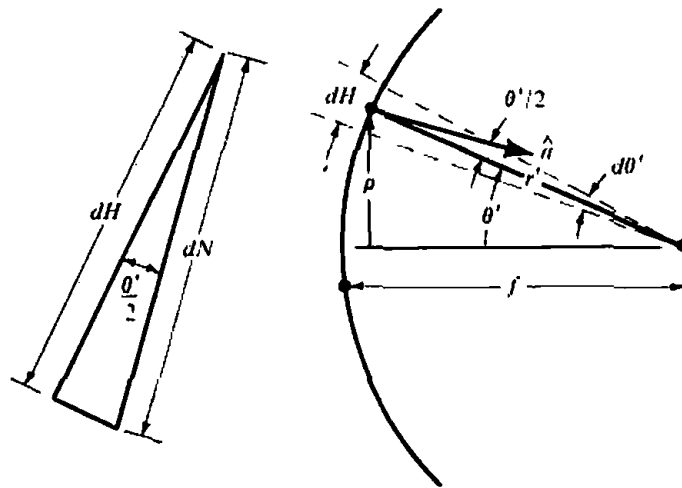
(b) Side-view

Figure 15.19   Projected cross section and side view of reflector.

$$E_\theta = -j\frac{\omega\mu}{4\pi r}e^{-jkr}\iint_{S_1} \hat{\mathbf{a}}_\theta \cdot \mathbf{J}_s e^{+jk\mathbf{r}'\cdot\hat{\mathbf{a}}_r}\, ds' \qquad (15\text{-}47\text{a})$$

$$E_\phi = -j\frac{\omega\mu}{4\pi r}e^{-jkr}\iint_{S_1} \hat{\mathbf{a}}_\phi \cdot \mathbf{J}_s e^{+jk\mathbf{r}'\cdot\hat{\mathbf{a}}_r}\, ds' \qquad (15\text{-}47\text{b})$$

According to the geometry of Figure 15.19

$$ds' = dW\, dN = (r'\,\sin\,\theta'\, d\phi')\left[r'\,\sec\left(\frac{\theta'}{2}\right)d\theta'\right]$$

$$= (r')^2\,\sin\,\theta'\,\sec\left(\frac{\theta'}{2}\right)d\theta'\, d\phi' \qquad (15\text{-}48)$$

since

$$dW = r' \sin \theta' \, d\phi' \tag{15-48a}$$

$$dH = -\hat{a}_r' \cdot d\,\mathbf{N} = -\hat{a}_r' \cdot \hat{n} \, dN$$

$$= -\hat{a}_r' \cdot \left[-\hat{a}_r' \cos\left(\frac{\theta'}{2}\right) + \hat{a}_\theta' \sin\left(\frac{\theta'}{2}\right) \right] dN = \cos\left(\frac{\theta'}{2}\right) dN \tag{15-48b}$$

$$dN = \sec\left(\frac{\theta'}{2}\right) dH = \sec\left(\frac{\theta'}{2}\right) r' \, d\theta' = r'\sec\left(\frac{\theta'}{2}\right) d\theta' \tag{15-48c}$$

Therefore, it can be shown that (15-47a) and (15-47b) can be expressed, with the aid of (15-37), (15-37a), and (15-48), as

$$\begin{bmatrix} E_\theta \\ E_\phi \end{bmatrix} = -j\frac{\omega\mu}{2\pi r}\sqrt{\frac{\epsilon}{\mu}}C_1 e^{-jkr}\begin{bmatrix} \hat{a}_\theta \cdot \mathbf{I} \\ \hat{a}_\phi \cdot \mathbf{I} \end{bmatrix}$$

$$= -j\frac{\omega\mu e^{-jkr}}{2\pi r}\left[\sqrt{\frac{\epsilon}{\mu}\frac{P_t}{2\pi}}\right]^{1/2}\begin{bmatrix} \hat{a}_\theta \cdot \mathbf{I} \\ \hat{a}_\phi \cdot \mathbf{I} \end{bmatrix} \tag{15-49}$$

where

$$\mathbf{I} = \mathbf{I}_t + \mathbf{I}_z \tag{15-49a}$$

$$\mathbf{I}_t = -\int_0^{2\pi}\int_0^{\theta_0} \hat{e}_r \cos\left(\frac{\theta'}{2}\right)\frac{\sqrt{G_f(\theta', \phi')}}{r'}e^{-jkr'[1 - \sin\theta'\sin\theta\cos(\phi' - \phi) - \cos\theta'\cos\theta]}$$

$$\times (r')^2 \sin\theta' \sec\left(\frac{\theta'}{2}\right) d\theta' \, d\phi' \tag{15-49b}$$

$$\mathbf{I}_z = -\hat{a}_z \int_0^{2\pi}\int_0^{\theta_0} (\hat{n} \cdot \hat{e}_r)\frac{\sqrt{G_f(\theta', \phi')}}{r'}e^{-jkr'[1 - \sin\theta'\sin\theta\cos(\phi' - \phi) - \cos\theta'\cos\theta]}$$

$$\times (r')^2 \sin\theta' \sec\left(\frac{\theta'}{2}\right) d\theta' \, d\phi' \tag{15-49c}$$

By comparing (15-49) with (15-35), the radiated field components formulated by the aperture distribution and current distribution methods lead to similar results provided the $\mathbf{I}_z$ contribution of (15-49c) is neglected. As the ratio of the aperture diameter to wavelength (d/λ) increases, the current distribution method results reduce to those of the aperture distribution and the angular pattern becomes more narrow.

For variations near the $\theta = \pi$ region, the $\mathbf{I}_z$ contribution becomes negligible because

$$\hat{a}_\theta \cdot [-\hat{a}_z(\hat{n} \cdot \hat{e}_r)] = [\hat{a}_x \sin\theta\cos\phi + \hat{a}_y \cos\theta\sin\phi - \hat{a}_z \sin\theta]$$

$$\cdot [-\hat{a}_z(\hat{n} \cdot \hat{e}_r)] = (\hat{n} \cdot \hat{e}_r)\sin\theta \tag{15-50a}$$

$$\hat{a}_\phi \cdot [-\hat{a}_z(\hat{n} \cdot \hat{e}_r)] = [-\hat{a}_x \sin\phi + \hat{a}_y \cos\phi] \cdot [-\hat{a}_z(\hat{n} \cdot \hat{e}_r)] = 0 \tag{15-50b}$$

F. Directivity and Aperture Efficiency

In the design of antennas, the directivity is a very important figure-of-merit. The purpose of this section will be to examine the dependence of the directivity and aperture efficiency on the primary-feed pattern $G_f(\theta', \phi')$ and f/d ratio (or the included angle $2\theta_0$) of the reflector. To simplify the analysis, it will be assumed that the feed

pattern $G_f(\theta', \phi')$ is circularly symmetric (not a function of ϕ') and that $G_f(\theta') = 0$ for $\theta' > 90°$.

The secondary pattern (formed by the surface of the reflector) is given by (15-49). Approximating the $\mathbf{I}$ of (15-49a) by $\mathbf{I}_r$, the total E-field in the $\theta = \pi$ direction is given by either E_θ or E_ϕ of (15-49). Assuming the feed is circularly symmetric, linearly polarized in the y-direction, and by neglecting cross-polarized contributions, it can be shown with the aid of (15-14a) that (15-49) reduces to

$$E(r, \theta = \pi) = -j\frac{2\omega\mu f}{r}\left[\sqrt{\frac{\epsilon}{\mu}}\frac{P_t}{2\pi}\right]^{1/2} e^{-jk(r+2f)} \int_0^{\theta_0} \sqrt{G_f(\theta')} \tan\left(\frac{\theta'}{2}\right) d\theta'$$

(15-51)

The power intensity (power/unit solid angle) in the forward direction $U(\theta = \pi)$ is given by

$$U(\theta = \pi) = \frac{1}{2}r^2 \sqrt{\frac{\epsilon}{\mu}} |E(r, \theta = \pi)|^2$$

(15-52)

which by using (15-51) reduces to

$$U(\theta = \pi) = \frac{16\pi^2}{\lambda^2}f^2 \frac{P_t}{4\pi}\left|\int_0^{\theta_0} \sqrt{G_f(\theta')} \tan\left(\frac{\theta'}{2}\right) d\theta'\right|^2$$

(15-52a)

The antenna directivity in the forward direction can be written, using (15-52a), as

$$D_0 = \frac{4\pi U(\theta = \pi)}{P_t} = \frac{U(\theta = \pi)}{P_t/4\pi} = \frac{16\pi^2}{\lambda^2}f^2\left|\int_0^{\theta_0} \sqrt{G_f(\theta')} \tan\left(\frac{\theta'}{2}\right) d\theta'\right|^2$$

(15-53)

The focal length is related to the angular spectrum and aperture diameter d by (15-25). Thus (15-53) reduces to

$$\boxed{D_0 = \left(\frac{\pi d}{\lambda}\right)^2 \left\{\cot^2\left(\frac{\theta_0}{2}\right)\left|\int_0^{\theta_0} \sqrt{G_f(\theta')} \tan\left(\frac{\theta'}{2}\right) d\theta'\right|^2\right\}}$$

(15-54)

The factor $(\pi d/\lambda)^2$ is the directivity of a uniformly illuminated constant phase aperture; the remaining part is the aperture efficiency defined as

$$\boxed{\epsilon_{ap} = \cot^2\left(\frac{\theta_0}{2}\right)\left|\int_0^{\theta_0} \sqrt{G_f(\theta')} \tan\left(\frac{\theta'}{2}\right) d\theta'\right|^2}$$

(15-55)

It is apparent by examining (15-55) that the aperture efficiency is a function of the subtended angle (θ_0) and the feed pattern $G_f(\theta')$ of the reflector. Thus for a given feed pattern, all paraboloids with the same f/d ratio have identical aperture efficiency.

To illustrate the variation of the aperture efficiency as a function of the feed pattern and the angular extent of the reflector, Silver [17] considered a class of feeds whose patterns are defined by

$$G_f(\theta') = \begin{cases} G_0^{(n)} \cos^n(\theta') & 0 \leq \theta' \leq \pi/2 \\ 0 & \pi/2 < \theta' \leq \pi \end{cases}$$

(15-56)

where $G_0^{(n)}$ is a constant for a given value of n. Although idealistic, these patterns were chosen because (1) closed form solutions can be obtained, and (2) they often

are used to represent a major part of the main lobe of many practical antennas. The intensity in the back region ($\pi/2 < \theta' \leq \pi$) was assumed to be zero in order to avoid interference between the direct radiation from the feed and scattered radiation from the reflector.

The constant $G_0^{(n)}$ can be determined from the relation

$$\oiint_S G_f(\theta') \, d\Omega = \oiint_S G_f(\theta') \sin \theta' \, d\theta' \, d\phi' = 4\pi \qquad (15\text{-}57)$$

which for (15-56) becomes

$$G_0^{(n)} \int_0^{\pi/2} \cos^n \theta' \sin \theta' \, d\theta' = 2 \Rightarrow G_0^{(n)} = 2(n + 1) \qquad (15\text{-}58)$$

Substituting (15-56) and (15-58) into (15-55) leads, for the even values of $n = 2$ through $n = 8$, to

$$\epsilon_{ap} (n = 2) = 24 \left\{ \sin^2 \left(\frac{\theta_0}{2} \right) + \ln \left[\cos \left(\frac{\theta_0}{2} \right) \right] \right\}^2 \cot^2 \left(\frac{\theta_0}{2} \right) \qquad (15\text{-}59a)$$

$$\epsilon_{ap} (n = 4) = 40 \left\{ \sin^4 \left(\frac{\theta_0}{2} \right) + \ln \left[\cos \left(\frac{\theta_0}{2} \right) \right] \right\}^2 \cot^2 \left(\frac{\theta_0}{2} \right) \qquad (15\text{-}59b)$$

$$\epsilon_{ap} (n = 6) = 14 \left\{ 2 \ln \left[\cos \left(\frac{\theta_0}{2} \right) \right] + \frac{[1 - \cos (\theta_0)]^3}{3} \right.$$

$$\left. + \frac{1}{2} \sin^2 (\theta_0) \right\}^2 \cot^2 \left(\frac{\theta_0}{2} \right) \qquad (15\text{-}59c)$$

$$\epsilon_{ap} (n = 8) = 18 \left\{ \frac{1 - \cos^4 (\theta_0)}{4} - 2 \ln \left[\cos \left(\frac{\theta_0}{2} \right) \right] - \frac{[1 - \cos (\theta_0)]^3}{3} \right.$$

$$\left. - \frac{1}{2} \sin^2 (\theta_0) \right\}^2 \cot^2 \left(\frac{\theta_0}{2} \right) \qquad (15\text{-}59d)$$

The variations of (15-59a)–(15-59d), as a function of the angular aperture of the reflector θ_0 or the f/d ratio, are shown plotted in Figure 15.20. It is apparent, from the graphical illustration, that for a given feed pattern (n = constant)

1. There is only one reflector with a given angular aperture or f/d ratio which leads to a maximum aperture efficiency.

2. Each maximum aperture efficiency is in the neighborhood of 82–83%.

3. Each maximum aperture efficiency, for any one of the given patterns, is almost the same as that of any of the others.

4. As the feed pattern becomes more directive (n increases), the angular aperture of the reflector that leads to the maximum efficiency is smaller.

The aperture efficiency is generally the product of the

1. fraction of the total power that is radiated by the feed, intercepted, and collimated by the reflecting surface (generally known as *spillover efficiency* ϵ_s)

2. uniformity of the amplitude distribution of the feed pattern over the surface of the reflector (generally known as *taper efficiency* ϵ_t)

3. phase uniformity of the field over the aperture plane (generally known as *phase efficiency* ϵ_p)
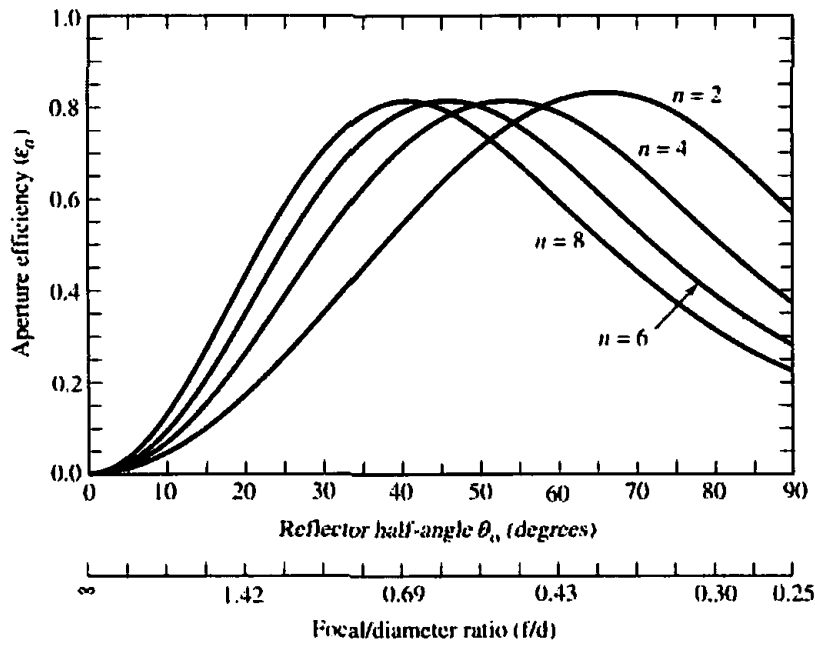
(a) Aperture efficiency
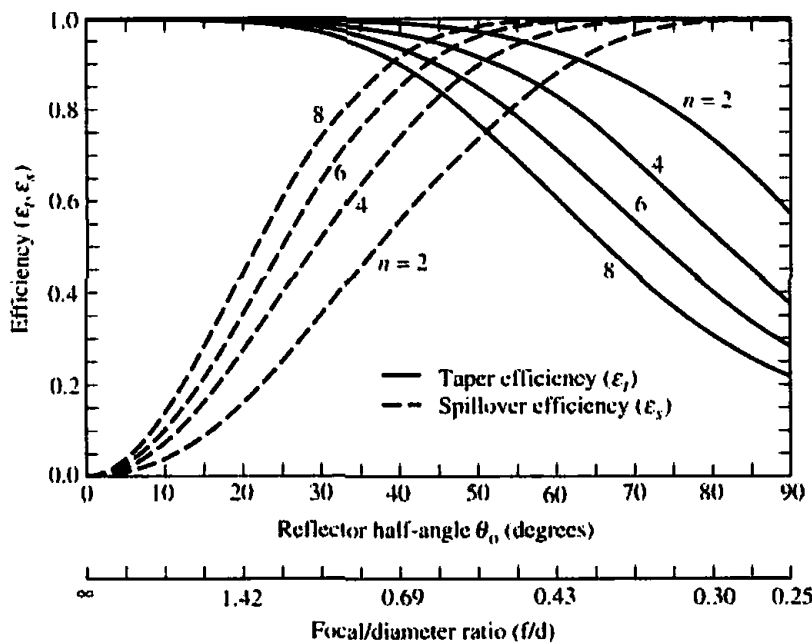
(b) Taper and spillover efficiencies

Figure 15.20 Aperture, and taper and spillover efficiencies as a function of the reflector half-angle θ_0 (or f/d ratio) for different feed patterns.

4. polarization uniformity of the field over the aperture plane (generally known as *polarization efficiency* ϵ_x)

5. *blockage efficiency* ϵ_b

6. *random error efficiency* ϵ_r over the reflector surface

Thus in general

$$\epsilon_{ap} = \epsilon_s \epsilon_t \epsilon_p \epsilon_x \epsilon_b \epsilon_r$$

(15-60)

For feeds with symmetrical patterns

$$
\epsilon_s = \frac{\int_0^{\theta_0} G_f(\theta') \sin \theta' \, d\theta'}{\int_0^{\pi} G_f(\theta') \sin \theta' \, d\theta'}
$$

(15-61)

$$
\epsilon_t = 2 \cot^2\left(\frac{\theta_0}{2}\right) \frac{\left| \int_0^{\theta_0} \sqrt{G_f(\theta')} \tan\left(\frac{\theta'}{2}\right) d\theta' \right|^2}{\int_0^{\theta_0} G_f(\theta') \sin \theta' \, d\theta'}
$$

(15-62)

which by using (15-25) can also be written as

$$
\epsilon_t = 32 \left(\frac{f}{d}\right)^2 \frac{\left| \int_0^{\theta_0} \sqrt{G_f(\theta')} \tan\left(\frac{\theta'}{2}\right) d\theta' \right|^2}{\int_0^{\theta_0} G_f(\theta') \sin \theta' \, d\theta'}
$$

(15-62a)

Thus

1. $100(1 - \epsilon_s)$ = percent power loss due to energy from feed spilling past the main reflector.

2. $100(1 - \epsilon_t)$ = percent power loss due to nonuniform amplitude distribution over the reflector surface.

3. $100(1 - \epsilon_p)$ = percent power loss if the field over the aperture plane is not in phase everywhere.

4. $100(1 - \epsilon_x)$ = percent power loss if there are cross-polarized fields over the antenna aperture plane.

5. $100(1 - \epsilon_b)$ = percent power loss due to blockage provided by the feed or supporting struts (also by subreflector for a dual reflector).

6. $100(1 - \epsilon_r)$ = percent power loss due to random errors over the reflector surface.

An additional factor that reduces the antenna gain is the attenuation in the antenna feed and associated transmission line.

For feeds with

1. symmetrical patterns
2. aligned phase centers
3. no cross-polarized field components
4. no blockage
5. no random surface error

the two main factors that contribute to the aperture efficiency are the spillover and nonuniform amplitude distribution losses. Because these losses depend primarily on the feed pattern, a compromise between spillover and taper efficiency must emerge. Very high spillover efficiency can be achieved by a narrow beam pattern with low
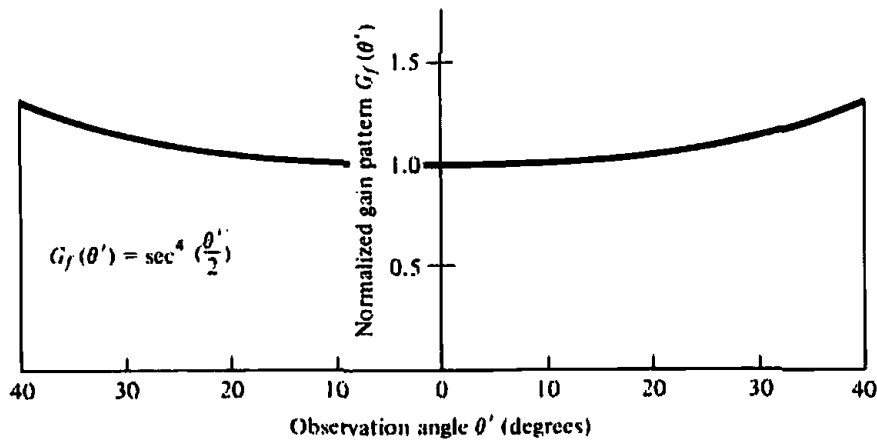
Figure 15.21 Normalized gain pattern of feed for uniform amplitude illumination of paraboloidal reflector with a total subtended angle of $80°$.

minor lobes at the expense of a very low taper efficiency. Uniform illumination and ideal taper efficiency can be obtained when the feed power pattern is

$$G_f(\theta') = \begin{cases} \sec^4\left(\dfrac{\theta'}{2}\right) & 0 \leq \theta' \leq \theta_0 \\ 0 & \theta' > \theta_0 \end{cases}$$

(15-63)

which is shown plotted in Figure 15.21. Although such a pattern is "ideal" and impractical to achieve, much effort has been devoted to develop feed designs which attempt to approximate it [14].

To develop guidelines for designing practical feeds which result in high aperture efficiencies, it is instructive to examine the relative field strength at the edges of the reflector's bounds ($\theta' = \theta_0$) for patterns that lead to optimum efficiencies. For the patterns of (15-56), when used with reflectors that result in optimum efficiencies as demonstrated graphically in Figure 15.20, the relative field strength at the edges of their angular bounds ($\theta' = \theta_0$) is shown plotted in Figure 15.22. Thus for $n = 2$ the field strength of the pattern at $\theta' = \theta_0$ is 8 dB down from the maximum. As the pattern becomes more narrow (n increases), the relative field strength at the edges for maximum efficiency is further reduced as illustrated in Figure 15.20. Since for $n = 2$ through $n = 10$ the field strength is between 8 to 10.5 dB down, for most practical feeds the figure used is 9–10 dB.

Another parameter to examine for the patterns of (15-56), when used with reflectors that lead to optimum efficiency, is the amplitude taper or illumination of the main aperture of the reflector which is defined as *the ratio of the field strength at the edge of the reflector surface to that at the vertex*. The aperture illumination is a function of the feed pattern and the f/d ratio of the reflector. To obtain that, the ratio of the angular variation of the pattern toward the two points $[G_f(\theta' = 0)/G_f(\theta' = \theta_0)]$ is multiplied by the space attenuation factor $(r_0/f)^2$, where f is the focal distance of the reflector and r_0 is the distance from the focal point to the edge of the reflector. For each of the patterns, the reflector edge illumination for maximum efficiency is 11 dB down from that at the vertex.

The results obtained with the idealized patterns of (15-56) should only be taken as typical, because it was assumed that

1. the field intensity for $\theta' > 90°$ was zero
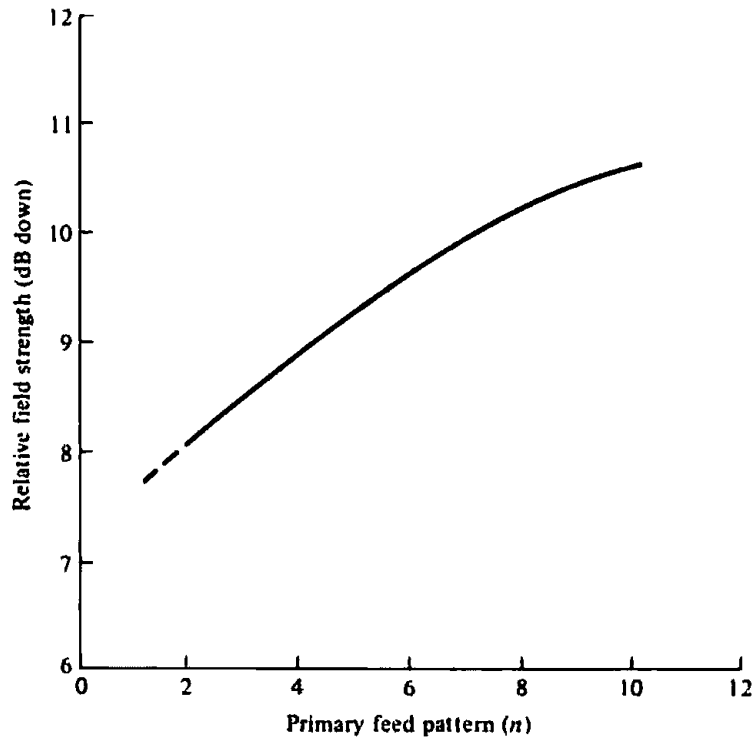2. the feed was placed at the phase center of the system

Figure 15.22 Relative field strength of feed pattern along reflector edge bounds as a function of primary feed pattern number (cos"θ). (SOURCE: S. Silver (ed.), *Microwave Antenna Theory and Design* (MIT Radiation Lab. Series, Vol. 12), McGraw-Hill, New York, 1949)

3. the patterns were symmetrical
4. there were no cross-polarized field components
5. there was no blockage
6. there were no random errors at the surface of the reflector

Each factor can have a significant effect on the efficiency, and each has received much attention which is well documented in the open literature [1].

In practice, maximum reflector efficiencies are in the 65–80% range. To demonstrate that, paraboloidal reflector efficiencies for square corrugated horns feeds were computed, and they are shown plotted in Figure 15.23. The corresponding amplitude taper and spillover efficiencies for the aperture efficiencies of Figures 15.20(a) and 15.23 are displayed, respectively, in Figures 15.20(b) and 15.24. For the data of Figures 15.23 and 15.24, each horn had aperture dimensions of $8\lambda \times 8\lambda$, their patterns were assumed to be symmetrical (by averaging the E- and H-planes), and they were computed using the techniques of Section 13.6. From the plotted data, it is apparent that the maximum aperture efficiency for each feed pattern is in the range of 74–79%, and that the product of the taper and spillover efficiencies is approximately equal to the total aperture efficiency.

We would be remiss if we left the discussion of this section without reporting the gain of some of the largest reflectors that exist around the world [23]. The gains are shown in Figure 15.25 and include the 1,000-ft (305-m) diameter spherical reflector [12] at Arecibo, Puerto Rico, the 100-m radio telescope [15] at Effelsberg, West Germany, the 64-m reflector [16] at Goldstone, California, the 22-m reflector at Krim, USSR, and the 12-m telescope at Kitt Peak, Arizona. The dashed portions of the curves indicate extrapolated values. For the Arecibo reflector, two curves are shown.
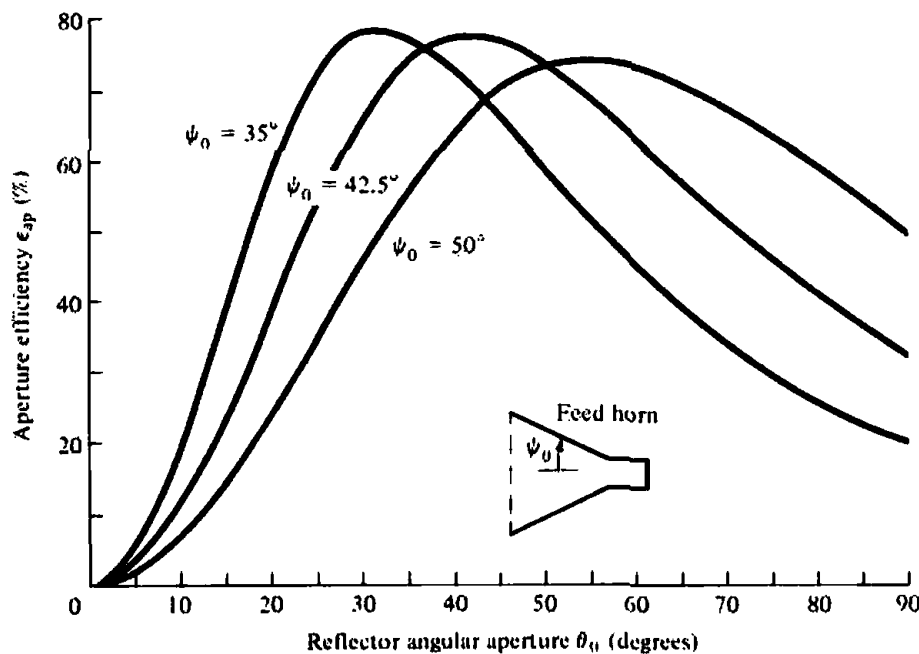
Figure 15.23 Parabolic reflector aperture efficiency as a function of angular aperture for $8\lambda \times 8\lambda$ square corrugated horn feed with total flare angles of $2\psi_0 = 70°, 85°,$ and $100°$.

The 215-m diameter curve is for a reduced aperture of the large reflector (305-m) for which a line feed at 1,415 MHz was designed [12].

G. Phase Errors

Any departure of the phase, over the aperture of the antenna, from uniform can lead to a significant diminution of its directivity [24]. For a paraboloidal reflector system, phase errors result from [17]

1. displacement (defocusing) of the feed phase center from the focal point

2. deviation of the reflector surface from a parabolic shape or random errors at the surface of the reflector

3. departure of the feed wave fronts from spherical shape

The defocusing effect can be reduced by first locating the phase center of the feed antenna and then placing it at the focal point of the reflector. In Chapter 13 (Section 13.10) it was shown that the phase center for horn antennas, which are widely utilized as feeds for reflectors, is located between the aperture of the horn and the apex formed by the intersection of the inclined walls of the horn [25].

Very simple expressions have been derived [24] to predict the loss in directivity for rectangular and circular apertures when the peak values of the aperture phase deviation is known. When the phase errors are assumed to be relatively small, it is not necessary to know the exact amplitude or phase distribution function over the aperture.

Assuming the maximum radiation occurs along the axis of the reflector, and that the maximum phase deviation over the aperture of the reflector can be represented by

$$|\Delta\phi(\rho)| = |\phi(\rho) - \overline{\phi(\rho)}| \leq m, \qquad \rho \leq a \qquad (15\text{-}64)$$

where $\phi(\rho)$ is the aperture phase function and $\overline{\phi(\rho)}$ is its average value, then the ratio of the directivity with (D) and without (D_0) phase errors can be written as [24]
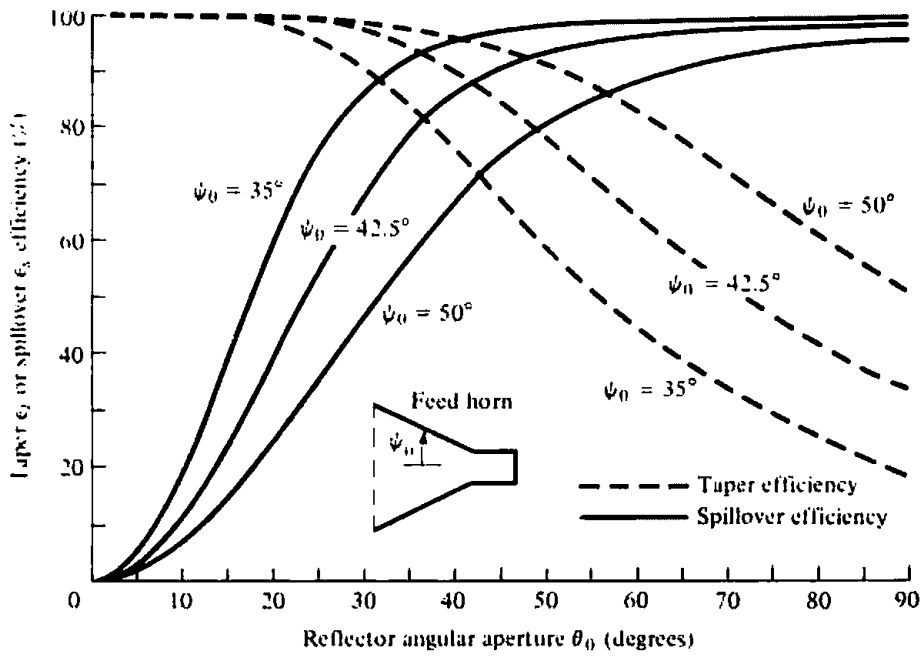
Figure 15.24 Parabolic reflector taper and spillover efficiencies as a function of reflector aperture for different corrugated horn feeds.
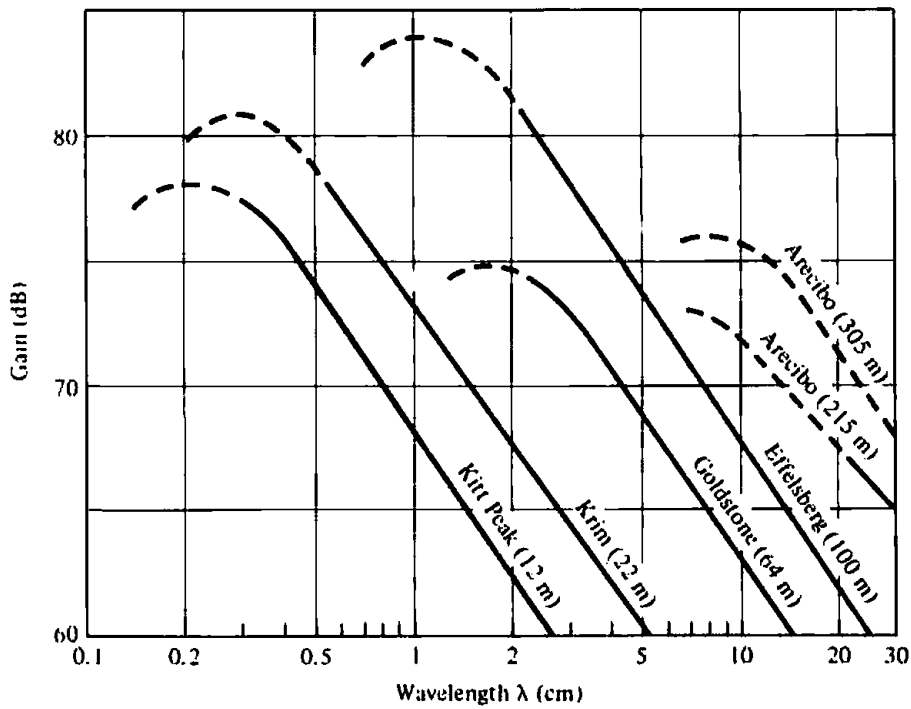

Figure 15.25 Gains of some worldwide large reflector antennas. (SOURCE: A. W. Love, Some Highlights in Reflector Antenna Development," *Radio Science*, Vol. 11, Nos. 8, 9, August–September 1976)

$$\frac{D}{D_0} = \frac{\text{directivity with phase error}}{\text{directivity without phase error}} \geq \left(1 - \frac{m^2}{2}\right)^2$$ (15-65)

and the maximum fractional reduction in directivity as

$$\frac{\Delta D}{D_0} = \frac{D_0 - D}{D_0} \leq m^2\left(1 - \frac{m^2}{4}\right)$$ (15-66)

Relatively simple expressions have also been derived [24] to compute the maximum possible change in half-power beamwidth.

Example 15.1

A 10-m diameter reflector, with an f/d ratio of 0.5, is operating at $f = 3$ GHz. The reflector is fed with an antenna whose primary pattern is symmetrical and which can be approximated by $G_f(\theta') = 6 \cos^2 \theta'$. Find its

    (a) aperture efficiency

    (b) overall directivity

    (c) spillover and taper efficiencies

    (d) directivity when the maximum aperture phase deviation is $\pi/8$ rad

SOLUTION

Using (15-24), half of the subtended angle of the reflector is equal to

$$\theta_0 = \tan^{-1}\left[\frac{0.5(0.5)}{(0.5)^2 - \frac{1}{16}}\right] = 53.13°$$

    (a) The aperture efficiency is obtained using (15-59a). Thus

$$\epsilon_{ap} = 24\{\sin^2(26.57°) + \ln[\cos(26.57°)]\}^2 \cot^2(26.57°)$$
$$= 0.75 = 75\%$$

which agrees with the data of Figure 15.20.

    (b) The overall directivity is obtained by (15-54), or

$$D = 0.75[\pi(100)]^2 = 74,022.03 = 48.69 \text{ dB}$$

    (c) The spillover efficiency is computed using (15-61) where the upper limit of the integral in the denominator has been replaced by $\pi/2$. Thus

$$\epsilon_s = \frac{\int_0^{53.13°} \cos^2 \theta' \sin \theta' \, d\theta'}{\int_0^{90°} \cos^2 \theta' \sin \theta' \, d\theta'} = \frac{2\cos^3 \theta'|_0^{53.13°}}{2\cos^3 \theta'|_0^{90°}} = 0.784 = 78.4\%$$

In a similar manner, the taper efficiency is computed using (15-62). Since the numerator in (15-62) is identical in form to the aperture efficiency of (15-55), the taper efficiency can be found by multiplying (15-59a) by 2 and dividing by the denominator of (15-62). Thus

$$\epsilon_t = \frac{2(0.75)}{1.568} = 0.9566 = 95.66\%$$

The product of ϵ_s and ϵ_t is equal to

$$\epsilon_s \epsilon_t = 0.784(0.9566) = 0.75$$

and it is identical to the total aperture efficiency computed above.

(d) The directivity for a maximum phase error of $m = \pi/8 = 0.3927$ rad can be computed using (15-65). Thus

$$\frac{D}{D_0} \geq \left(1 - \frac{m^2}{2}\right)^2 = \left[1 - \frac{(0.3927)^2}{2}\right]^2 = 0.8517 = -0.69 \text{ dB}$$

or $D \geq 0.8517 D_0 = 0.8517(74,022.03) = 63,046.94 = 48.0$ dB

Surface roughness effects on the directivity of the antenna were first examined by Ruze [26] where he indicated that for any reflector antenna there is a wavelength (λ_{max}) at which the directivity reaches a maximum. This wavelength depends on the RMS deviation (σ) of the reflector surface from an ideal paraboloid. For a random roughness of Gaussian distribution, with correlation interval large compared to the wavelength, they are related by

$$\lambda_{max} = 4\pi\sigma \tag{15-67}$$

Thus the directivity of the antenna, given by (15-54), is modified to include surface roughness and can be written as

$$D = \left(\frac{\pi d}{\lambda}\right)^2 \epsilon_{ap} e^{-(4\pi\sigma/\lambda)^2} \tag{15-68}$$

Using (15-67), the maximum directivity of (15-68) can be written as

$$\boxed{D_{max} = 10^{2q} \epsilon_{ap}\left(\frac{e^{-1}}{16}\right)} \tag{15-69}$$

where q is the index of smoothness defined by

$$\frac{d}{\sigma} = 10^{+q} \tag{15-70}$$

In decibels, (15-69) reduces to

$$\boxed{D_{max}(\text{dB}) = 20q - 16.38 + 10\log_{10}(\epsilon_{ap})} \tag{15-71}$$

For an aperture efficiency of unity $(\epsilon_{ap} = 1)$, the directivity of (15-68) is plotted in Figure 15.26, as a function of (d/λ), for values of $q = 3.5, 4.0,$ and 4.5. It is apparent that for each value of q and a given reflector diameter d, there is a maximum wavelength where the directivity reaches a maximum value. This maximum wavelength is given by (15-67).

H. Feed Design

The widespread use of paraboloidal reflectors has stimulated interest in the development of feeds to improve the aperture efficiency and to provide greater discrimination
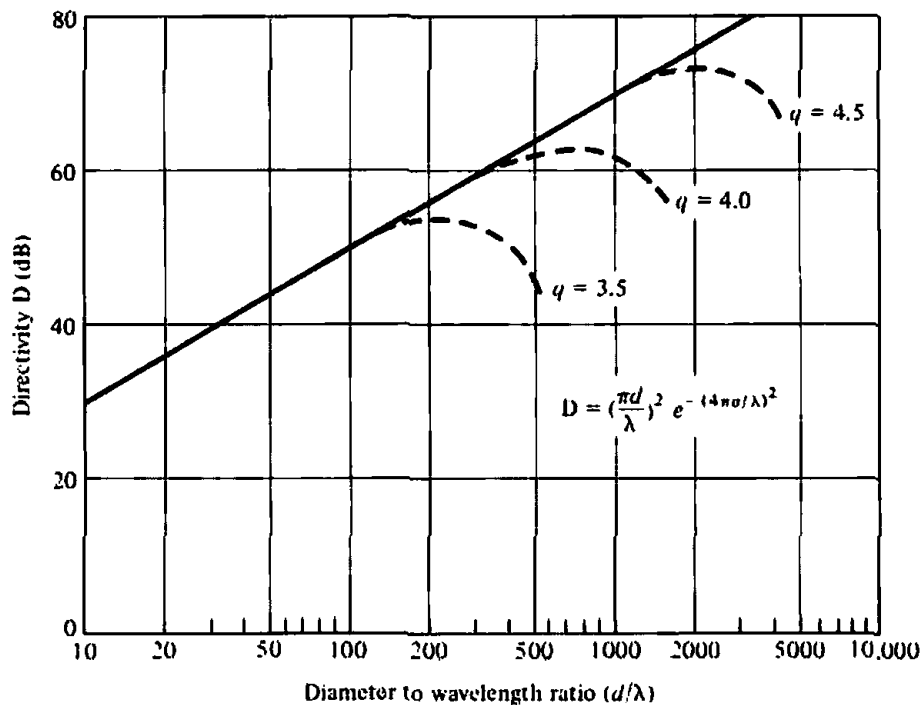
Figure 15.26 Reflector surface roughness effects on antenna directivity. (SOURCE: A. W. Love, "Some Highlights in Reflector Antenna Development," *Radio Science*, Vol. 11, Nos 8, 9, August–September 1976)

against noise radiation from the ground. This can be accomplished by developing design techniques that permit the synthesis of feed patterns with any desired distribution over the bounds of the reflector, rapid cutoff at its edges, and very low minor lobes in all the other space. In recent years, the two main problems that concerned feed designers were aperture efficiency and low cross-polarization.

In the receiving mode, an ideal feed and a matched load would be one that would absorb all the energy intercepted by the aperture when uniform and linearly polarized plane waves are normally incident upon it. The feed field structure must be made to match the focal region field structure formed by the reflecting, scattering, and diffracting characteristics of the reflector. By reciprocity, an ideal feed in the transmitting mode would be one that radiates only within the solid angle of the aperture and establishes within it an identical outward traveling wave. For this ideal feed system, the transmitting and receiving mode field structures within the focal region are identical with only the direction of propagation reversed.

An optical analysis indicates that the focal region fields, formed by the reflection of linearly polarized plane waves incident normally on an axially symmetric reflector, are represented by the well-known Airy rings described mathematically by the amplitude distribution intensity of $[2J_1(u)/u]^2$. This description is incomplete, because it is a scalar solution, and it does not take into account polarization effects. In addition, it is valid only for reflectors with large f/d ratios, which are commonly used in optical systems, and it would be significantly in error for reflectors with f/d ratios of 0.25 to 0.5, which are commonly used in microwave applications.

A vector solution has been developed [27] which indicates that the fields near the focal region can be expressed by hybrid TE and TM modes propagating along the axis of the reflector. This representation provides a clear physical picture for the understanding of the focal region field formation. The boundary conditions of the hybrid modes indicate that these field structures can be represented by a spectrum of

hybrid waves that are linear combinations of TE_{1n} and TM_{1n} modes of circular waveguides.

A single hollow pipe cannot simultaneously satisfy both the TE and TM modes because of the different radial periodicities. However, it has been shown that $\lambda/4$ deep annular slots on the inner surface of a circular pipe force the boundary conditions on E and H to be the same and provide a single anisotropic reactance surface which satisfies the boundary conditions on both TE and TM modes. This provided the genesis of hybrid mode waveguide radiators [28] and corrugated horns [29]. Corrugated horns, whose aperture size and flare angle are such that at least 180° phase error over their aperture is assured, are known as "scalar" horns [30]. Design data for uncorrugated horns that can be used to maximize the aperture efficiency or to produce maximum power transmission to the feed have been calculated [31] and are shown in graphical form in Figure 15.27.

A software package for computer-aided analysis and design of reflector antennas has been developed [32]. The program computes the radiation of parabolic and spherical reflectors. In addition it provides spatial and spectral methods to compute radiation due to an aperture distribution. The software package can also be used to investigate the directivity, beamwidth, sidelobe level, polarization, and near-to-far-zone fields. The program can be obtained through CAEME. Center of Excellence for Multimedia.

15.4.2 Cassegrain Reflectors

To improve the performance of large ground-based microwave reflector antennas for satellite tracking and communication, it has been proposed that a two-reflector system
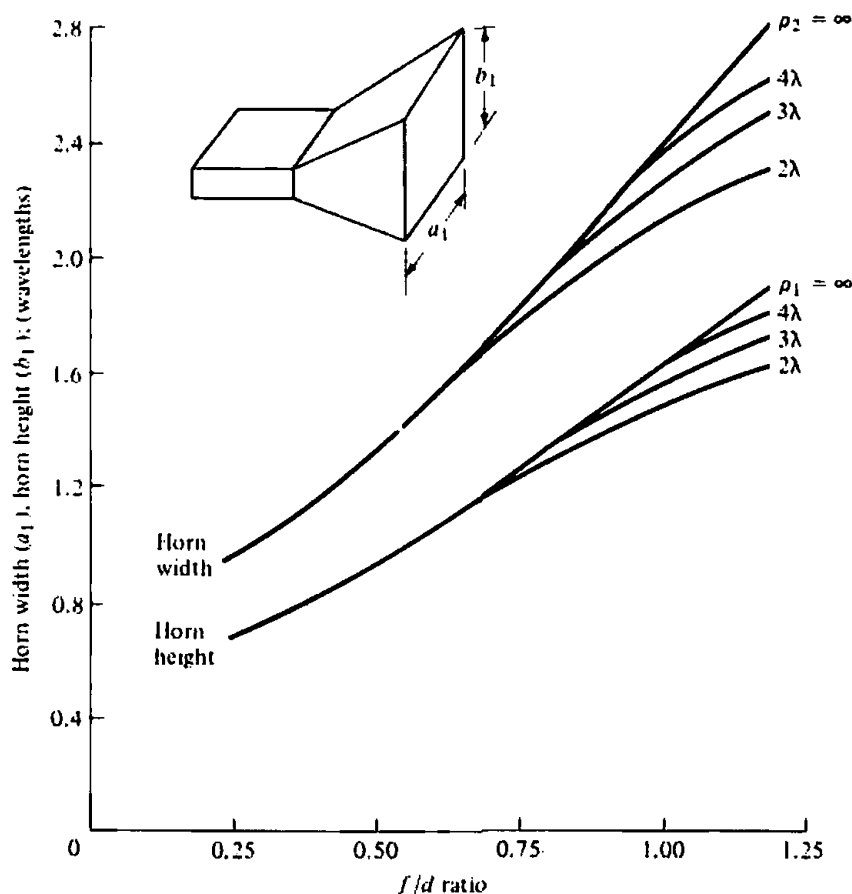

Figure 15.27 Optimum pyramidal horn dimensions versus f/d ratio for various horn lengths.

be utilized. The arrangement suggested was the Cassegrain dual-reflector system [33] of Figure 15.1(d), which was often utilized in the design of optical telescopes and it was named after its inventor. To achieve the desired collimation characteristics, the larger (main) reflector must be a paraboloid and the smaller (secondary) a hyperboloid. The use of a second reflector, which is usually referred to as the subreflector or subdish, gives an additional degree of freedom for achieving good performance in a number of different applications. For an accurate description of its performance, diffraction techniques must be used to take into account diffractions from the edges of the subreflector, especially when its diameter is small [34].

In general, the Cassegrain arrangement provides a variety of benefits, such as the

1. ability to place the feed in a convenient location
2. reduction of spillover and minor lobe radiation
3. ability to obtain an equivalent focal length much greater than the physical length
4. capability for scanning and/or broadening of the beam by moving one of the reflecting surfaces

To achieve good radiation characteristics, the subreflector or subdish must be several, at least a few, wavelengths in diameter. However, its presence introduces shadowing which is the principal limitation of its use as a microwave antenna. The shadowing can significantly degrade the gain of the system, unless the main reflector is several wavelengths in diameter. Therefore the Cassegrain is usually attractive for applications that require gains of 40 dB or greater. There are, however, a variety of techniques that can be used to minimize aperture blocking by the subreflector. Some of them are [33] (1) minimum blocking with simple Cassegrain, and (2) twisting Cassegrains for least blocking.

The first comprehensive published analysis of the Cassegrain arrangement as a microwave antenna is that by Hannan [33]. He uses geometrical optics to derive the geometrical shape of the reflecting surfaces, and he introduces the equivalence concepts of the virtual feed and the equivalent parabola. Although his analysis does not predict fine details, it does give reasonably good results. Refinements to his analysis have been introduced [34]–[36].

To improve the aperture efficiency, suitable modifications to the geometrical shape of the reflecting surfaces have been suggested [37]–[39]. The reshaping of the reflecting surfaces is used to generate desirable amplitude and phase distributions over one or both of the reflectors. The resultant system is usually referred to as *shaped* dual-reflector. The reflector antenna of Figure 15.9 is such a system. Shaped reflector surfaces, generated using analytical models, are illustrated in [39]. It also has been suggested [35] that a flange is placed around the subreflector to improve the aperture efficiency.

Since many reflectors have dimensions and radii of curvature large compared to the operating wavelength, they were traditionally designed based on geometrical optics (GO) [39]. Both the single- and double-reflector (Cassegrain) systems were designed to convert a spherical wave at the source (focal point) into a plane wave. Therefore the reflecting surfaces of both reflector systems were primarily selected to convert the phase of the wavefront from spherical to planar. However, because of the variable radius of curvature at each point of reflection, the magnitude of the reflected field is also changed due to spatial attenuation or amplitude spreading factor [40] or divergence factor (4-131) of Section 4.8.3, which are functions of the radius of curvature of the surface at the point of reflection. This ultimately leads to amplitude taper of

(a) Input and output bundle of rays.

(b) Specified feed and prescribed output.
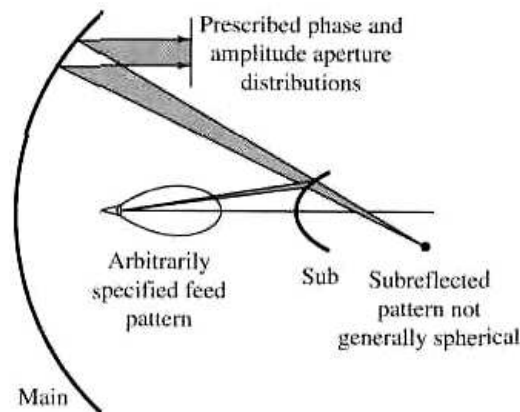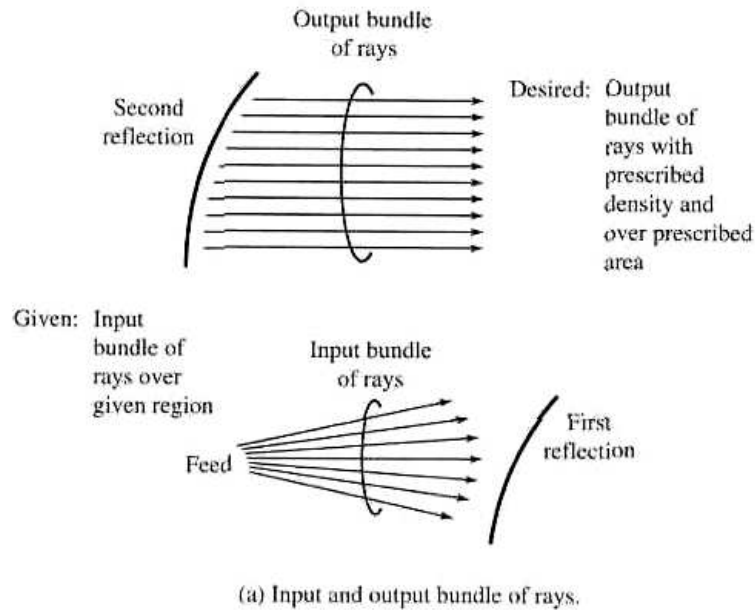
Figure 15.28 Geometrical optics for the reshaping and synthesis of the reflectors of a Cassegrain system. (SOURCE: R. Mittra and V. Galindo-Israel "Shaped Dual Reflector Synthesis," *IEEE Antennas and Propagation Society Newsletter*, Vol. 22, No. 4, pp. 5–9, August 1980. © (1980) IEEE)

the wavefront at the aperture plane. This is usually undesirable, and it can sometimes be compensated to some extent by the design of the pattern of the feed element or of the reflecting surface.

For a shaped-dual reflector system, there are two surfaces or degrees of freedom that can be utilized to compensate for any variations in the phase and amplitude of the field at the aperture plane. To determine how each surface may be reshaped to control the phase and/or amplitude of the field at the aperture plane, let us use geometrical optics and assume that the field radiated by the feed (pattern) is represented, both in amplitude and phase, by a bundle of rays which has a well-defined periphery. This bundle of rays is initially intecepted by the subreflector and then by the main reflector. Ultimately the output, after two reflections, is also a bundle of rays with prescribed phase and amplitude distributions, and a prescribed periphery, as shown in Figure 15.28(a) [41]. It has been shown in [42] that for a two-reflector

system with high magnification (i.e., large ratio of main reflector diameter to sub-reflector diameter) that over the aperture plane the

(a)   amplitude distribution is controlled largely by the subreflector curvature.

(b)   phase distribution is controlled largely by the curvature of the main reflector.

Therefore in a Cassegrain two-reflector system the reshaping of the paraboloid main reflector can be used to optimize the phase distribution while the reshaping of the hyperboloid subreflector can be used to control the amplitude distribution. This was used effectively in [42] to design a shaped two-reflector system whose field reflected by the subreflector had a nonspherical phase but a $\csc^4(\theta/2)$ amplitude pattern. However, the output from the main reflector had a perfect plane wave phase front and a very good approximate uniform amplitude distribution, as shown in Figure 15.28(b).

Because a comprehensive treatment of this arrangement can be very lengthy, only a brief introduction of the system will be presented here. The interested reader is referred to the referenced literature.

A. Classical Cassegrain Form

The operation of the Cassegrain arrangement can be introduced by referring to Figure 15.1(d) and assuming the system is operating in the receiving or transmitting mode. To illustrate the principle, a receiving mode is adopted.

Let us assume that energy, in the form of parallel rays, is incident upon the reflector system. Energy intercepted by the main reflector, which has a large concave surface, is reflected toward the subreflector. Energy collected by the convex surface of the subdish is reflected by it, and it is directed toward the vertex of the main dish. If the incident rays are parallel, the main reflector is a paraboloid, and the subreflector is a hyperboloid, then the collected bundle of rays is focused at a single point. The receiver is then placed at this focusing point.

A similar procedure can be used to describe the system in the transmitting mode. The feed is placed at the focusing point, and it is usually sufficiently small so that the subdish is located in its far-field region. In addition, the subreflector is large enough that it intercepts most of the radiation from the feed. Using the geometrical arrangement of the paraboloid and the hyperboloid, the rays reflected by the main dish will be parallel. The amplitude taper of the emerging rays is determined by the feed pattern and the tapering effect of the geometry.

The geometry of the classical Cassegrain system, employing a concave paraboloid as the main dish and a convex hyperboloid as the subreflector, is simple and it can be described completely by only four independent parameters (two for each reflector). The analytical details can be found in [33].

To aid in the understanding and in predicting the essential performance of a Cassegrain, the concept of virtual feed [33] is useful. By this principle, the real feed and the subreflector are replaced by an equivalent system which consists of a virtual feed located at the focal point of the main reflector, as shown by the dashed lines of Figure 15.29(a). For analysis purposes then, the new system is a single-reflector arrangement with the original main dish, a different feed, and no subreflector.

The configuration of the virtual feed can be determined by finding the optical image of the real feed. This technique is only accurate when examining the effective aperture of the feed and when the dimensions of the real and virtual feeds are larger than a wavelength. In fact, for the classical Cassegrain arrangement of Figure 15.29(a), the virtual feed has a smaller effective aperture, and a corresponding broader beamwidth, than the real feed. The increase in beamwidth is a result of the convex curvature

(a) Virtual-feed

(b) Equivalent-parabola
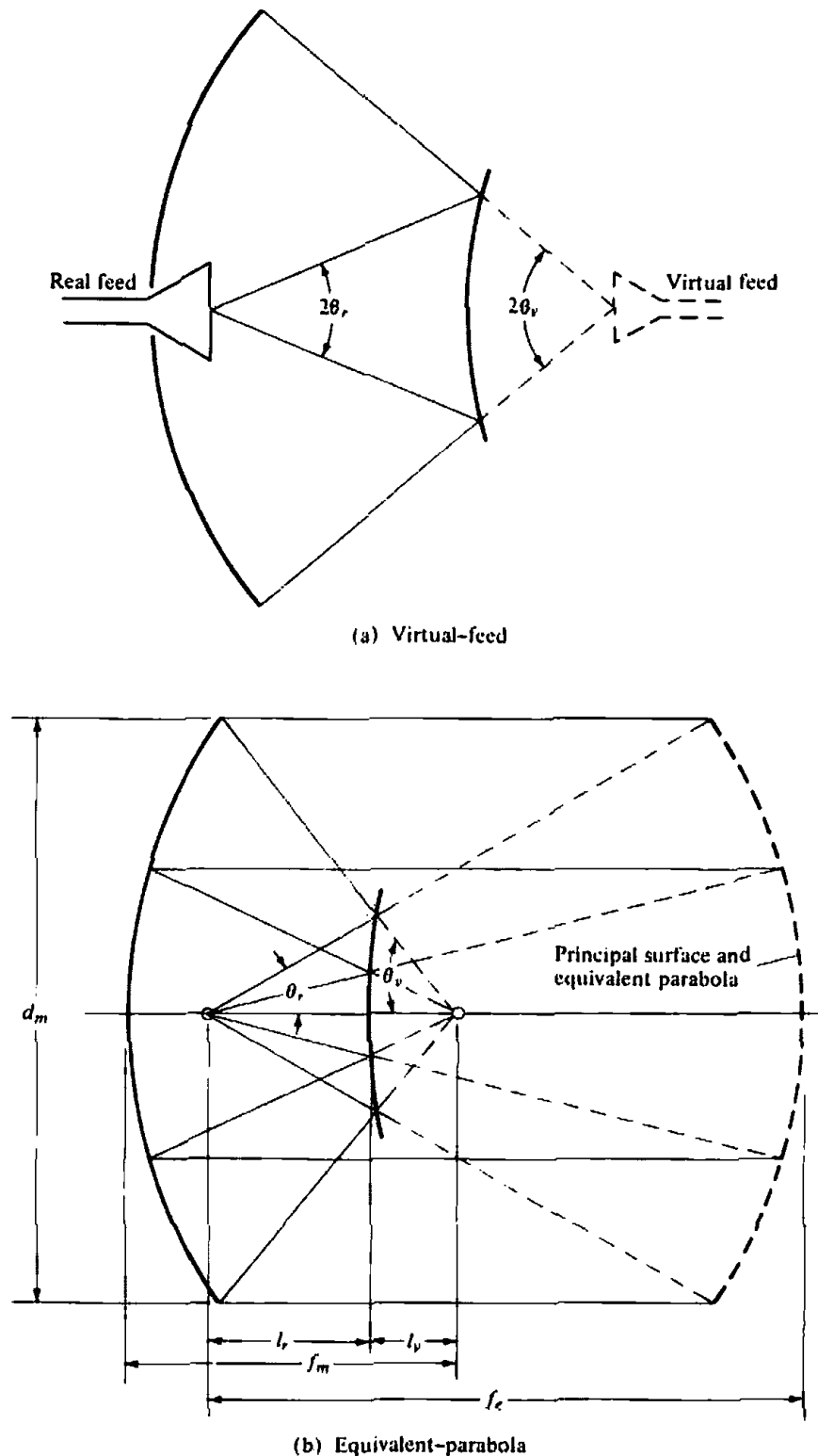
Figure 15.29 Virtual-feed and equivalent parabola concepts. (SOURCE: P. W. Hannan, "Microwave Antennas Derived from the Cassegrain Telescope." *IRE Trans. Antennas Propagat.* Vol. AP-9, No. 2, March 1961. © (1961) IEEE)

of the subreflector, and it can be determined by equating the ratio of the virtual to real-feed beamwidths to the ratio of the angles θ_v/θ_r.

The ability to obtain a different effective aperture for the virtual feed as compared to that of the real feed is useful in many applications such as in a monopulse antenna [33]. To maintain efficient and wideband performance and effective utilization of the

main aperture, this system requires a large feed aperture, a corresponding long focal length, and a large antenna structure. The antenna dimensions can be maintained relatively small by employing the Cassegrain configuration which utilizes a large feed and a short focal length for the main reflector.

Although the concept of virtual feed can furnish useful qualitative information for a Cassegrain system, it is not convenient for an accurate quantitative analysis. Some of the limitations of the virtual feed concept can be overcome by the concept of the *equivalent parabola* [33].

By the technique of the equivalent parabola, the main dish and the subreflector are replaced by an equivalent focusing surface at a certain distance from the real focal point. This surface is shown dashed in Figure 15.29(b), and it is defined as [33] "the locus of intersection of incoming rays parallel to the antenna axis with the extension of the corresponding rays converging toward the real focal point." Based on simple geometrical optics ray tracing, the equivalent focusing surface for a Cassegrain configuration is a paraboloid whose focal length equals the distance from its vertex to the real focal point. This equivalent system also reduces to a single-reflector arrangement, which has the same feed but a different main reflector, and it is accurate when the subreflector is only a few wavelengths in diameter. More accurate results can be obtained by including diffraction patterns. It also has the capability to focus toward the real focal point an incoming plane wave, incident from the opposite direction, in exactly the same manner as the actual main dish and the subreflector.

B. Cassegrain and Gregorian Forms

In addition to the classical Cassegrain forms, there are other configurations that employ a variety of main reflector and subreflector surfaces and include concave, convex, and flat shapes [33]. In one form, the main dish is held invariant while its feed beamwidth progressively increases and the axial dimensions of the antenna progressively decrease. In another form, the feed beamwidth is held invariant while the main reflector becomes progressively flatter and the axial dimensions progressively increase.

A series of configurations in which the feed beamwidth is progressively increased, while the overall antenna dimensions are held fixed, are shown in Figure 15.30. The first five are referred to as Cassegrain forms while the last two are Gregorian forms, whose configurations are similar to the Gregorian telescope. A number of parameter ranges, along with distinguishing characteristics, are indicated alongside each configuration sketch. The main dish for the fourth configuration has degenerated to a flat contour, the subreflector to a parabolic contour, and they can be separated by distances where the ray-tracing approximation is valid. For the fifth configuration, the subreflector has degenerated to a ridiculous extreme concave elliptical contour and the main dish to a convex parabolic form, with the former being larger than the latter.

For the last two configurations, which are referred to as Gregorian forms, the focal point of the main dish has moved to the region between the two dishes and the subreflector has attained a concave elliptical contour. When the overall size and the feed beamwidth of the classical Gregorian are identical to those of the classical Cassegrain, the Gregorian form requires a shorter focal length for the main dish. The feed for the second of the Gregorian forms has moved to a location between the focus of the main dish and the subreflector while the main dish has kept the same dimensions as the first form. In general, this configuration has several major disadvantages that make it unattractive for many antenna applications.

From the data in Figure 15.30, the relative sizes of the effective apertures of the virtual and real feeds can be inferred. When the subreflector is flat, the real and virtual feeds are identical. The virtual feeds of the Cassegrain configurations, which have a

Illustration	θ_v/θ_r and l_e/l_m	l_m and l_c	e
Cassegrain reflector forms — PAR, HYP — Convex subdish (classical form)	>1	>0	>1
PAR, FLAT, PAR — Flat subdish	1	>0	∞
PAR, PAR, HYP — Concave subdish	<1 >0	>0	< −1
FLAT PAR, PAR — Flat main dish	0	∞	1
PAR, ELL, PAR — Convex main dish	<0 > −1	<0	<0 > −1
Gregorian reflector forms — PAR, ELL, PAR — Feed in rear (classical form)	>1	>0	>0 <1
PAR, PAR, ELL — Feed in front of main dish focus	<1	<0	>0 <1

Figure 15.30 Series of Cassegrain and Gregorian reflector forms. (SOURCE: P. W. Hannan, "Microwave Antennas Derived from the Cassegrain Telescope." *IRE Trans. Antennas Propagat.*, Vol. AP-9, No. 2, March 1961. © (1961) IEEE)

concave subreflector, possess smaller beamwidths and larger effective apertures than their corresponding real feeds. However, the virtual feed of the classical Gregorian configuration, which also has a concave subreflector, possesses an effective aperture which is smaller than that of the real feed.

The equivalent parabola concept is applicable to all the Cassegrain and Gregorian forms, and they are shown dashed in Figure 15.30. The classical Cassegrain and Gregorian configurations have equivalent focal lengths which are greater than the focal lengths of the corresponding main dishes. For the Cassegrain arrangement with the flat subreflector, the equivalent focal length is equal to the focal length of the main dish. In general, the equivalent focal lengths of the Cassegrain configurations which have a concave subreflector are shorter than the focal lengths of their corresponding main dishes. For the configuration with the flat main dish, the equivalent parabola is identical with the subreflector.

The equivalent parabola concept can also be used to determine the amplitude taper across the aperture of a Cassegrain arrangement. As for the front-fed configuration, the amplitude taper or aperture illumination is determined by the radiation pattern of the feed modified by the space attenuation factor of the reflector. The amplitude taper of a Cassegrain configuration is identical to that of a front-fed arrangement whose feed is the actual feed and whose focal length is the equivalent focal length. In other words, the process is identical to that of a front-fed configuration except that the equivalent f_e/d ratio is used.

15.5   SPHERICAL REFLECTOR

The discussion and results presented in the previous sections illustrate that a paraboloidal reflector is an ideal collimating device. However, despite all of its advantages and many applications it is severely handicapped in angular scanning. Although scanning can be accomplished by (1) mechanical rotation of the entire structure, and (2) displacement of the feed alone, it is thwarted by the large mechanical moment of inertia in the first case and by the large coma and astigmatism in the second. By contrast, the spherical reflector can make an ideal wide-angle scanner because of its perfectly symmetrical geometrical configuration. However, it is plagued by poor inherent collimating properties. If, for example, a point source is placed at the focus of the sphere, it does not produce plane waves. The departure of the reflected wavefront from a plane wave is known as spherical aberration, and it depends on the diameter and focal length of the sphere. By reciprocity, plane waves incident on a spherical reflector surface parallel to its axis do not coverge at the focal point. However a spherical reflector has the capability of focusing plane waves incident at various angles by translating and orientating the feed and by illuminating different parts of the structural geometry. The 1,000-ft diameter reflector [12] at Arecibo, Puerto Rico is a spherical reflector whose surface is built into the earth and the scanning is accomplished by movement of the feed.

The focusing characteristics of a typical spherical reflector is illustrated in Figure 15.31 for three rays. The point F in the figure is the paraxial focus, and it is equal to one-half the radius of the sphere. The caustic* surface is an epicycloid and is generated

---

*A caustic is a point, a line, or a surface through which all the rays in a bundle pass and where the intensity is infinite. The caustic also represents the geometrical loci of all the centers of curvature of the wave surfaces. Examples of it include the focal line for cylindrical parabolic reflector and the focal point of a paraboloidal reflector.
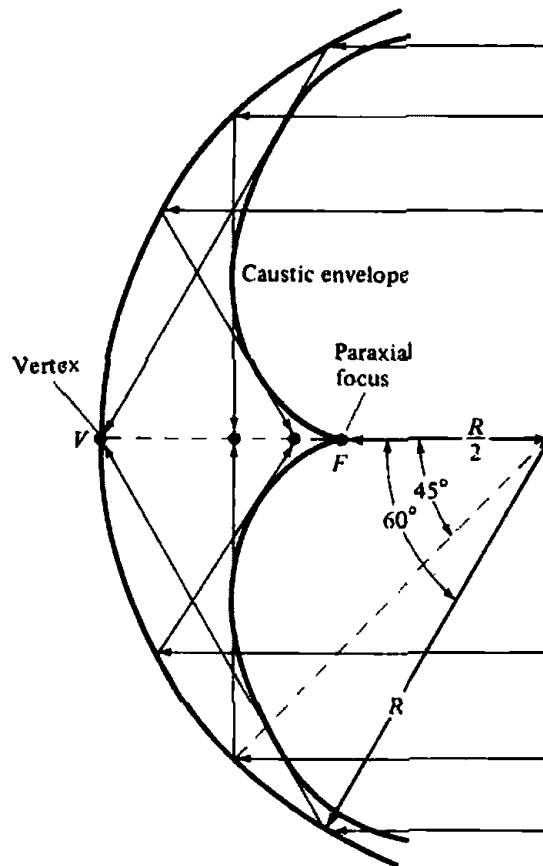
Figure 15.31 Spherical reflector geometry and rays that form a caustic.

by the reflection of parallel rays. A degenerate line FV of this caustic is parallel to the incident rays and extends from the paraxial focus to the vertex of the reflector. If one draws a ray diagram of plane waves incident within a 120° cone, it will be shown that all energy must pass through the line FV. Thus, the line FV can be used for the placement of the feed for the interception of plane waves incident parallel to the axial line. It can thus be said that a spherical reflector possesses a line focus instead of a point. However, amplitude and phase corrections must be made in order to realize maximum antenna efficiency.

Ashmead and Pippard [43] proposed to reduce spherical aberration and to minimize path error by placing a point source feed not at the paraxial focus F (half radius of the sphere), as taught in optics, but displaced slightly toward the reflector. For an aperture of diameter d, the correct location for placing a point source is a distance f_0 from the vertex such that the maximum path error value is [43]

$$\boxed{\Delta_{max} \simeq \frac{d^4}{2000 f_0^3}}$$

(15-72)

and the maximum phase error does not differ from a paraboloid by more than one-eighth of a wavelength. This, however, leads to large f/d and to poor area utilization. A similar result was obtained by Li [44]. He stated that the total phase error (sum of maximum absolute values of positive and negative phase errors) over an aperture of radius a is least when the phase error at the edge of the aperture is zero. Thus the optimum focal length is

$$f_{op} = \frac{1}{4}(R + \sqrt{R^2 - a^2})$$

(15-73)

where

R = radius of the spherical reflector

a = radius of the utilized aperture

Thus when $R = 2a$, the optimum focal length is $0.4665R$ and the corresponding total phase error, using the formula found in [44], is $0.02643(R/\lambda)$ rad. Even though the optimum focal length leads to minimum total phase error over a prescribed aperture, it does not yield the best radiation pattern when the illumination is not uniform. For a tapered amplitude distribution, the focal length that yields the best radiation pattern will be somewhat longer, and in practice, it is usually determined by experiment. Thus for a given maximum aperture size there exists a maximum value of total allowable phase error, and it is given by [44]

$$\left(\frac{a}{R}\right)^4_{max} = 14.7\frac{(\Delta/\lambda)_{total}}{(R/\lambda)}$$

(15-74)

where (Δ/λ) is the total phase error in wavelengths.

Example 15.2

A spherical reflector has a 10-ft diameter. If at 11.2 GHz the maximum allowable phase error is $\lambda/16$, find the maximum permissible aperture.

SOLUTION

At $f = 11.2$ GHz

$$\lambda = 0.08788 \text{ ft}$$

$$\left(\frac{a}{R}\right)^4_{max} = 14.7\left(\frac{1/16}{56.8957}\right) = 0.01615$$

$$a^4 \approx 10.09$$

$$a = 1.78 \text{ ft}$$

To overcome the shortcoming of a point feed and minimize spherical aberration, Spencer, Sletten, and Walsh [45] were the first to propose the use of a line source feed. Instead of a continuous line source, a set of discrete feed elements can be used to reduce spherical aberration when they are properly placed along the axis in the vicinity of the paraxial focus. The number of elements, their position, and the portion of the reflector surface which they illuminate is dictated by the allowable wavefront distortion, size, and curvature of the reflector. This is shown in Figure 15.32 [46]. A single feed located near the paraxial focus will illuminate the central portion of the reflector. If the reflector is large, additional feed elements along the axis toward the
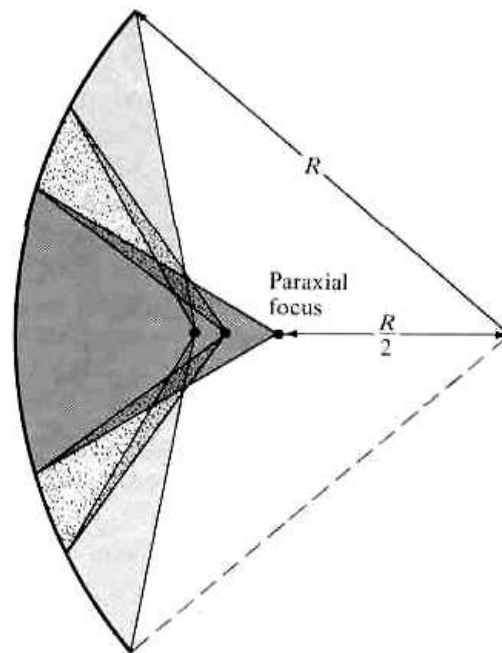
Figure 15.32 Reflector illumination by feed sections placed between paraxial focus and vertex. (SOURCE: A. C. Schell, "The Diffraction Theory of Large-Aperture Spherical Reflector Antennas," *IRE Trans. Antennas Propagat.*, Vol. AP-11, No. 4, July 1963. © (1963) IEEE)

vertex will be needed to minimize the phase errors in the aperture. The ultimate feed design will be a compromise between a single element and a line-source distribution.

An extensive effort has been placed on the analysis and experiment of spherical reflectors, and most of it can be found well documented in a book of reprinted papers [1]. In addition, a number of two-dimensional patterns and aperture plane constant amplitude contours, for symmetrical and offset feeds, have been computed [20].

References

1. A. W. Love (ed.), *Reflector Antennas,* IEEE Press, New York, 1978.
2. Y. Obha, "On the Radiation of a Corner Reflector Finite in Width," *IEEE Trans. Antennas Propagat.,* Vol. AP-11, No. 2, pp. 127–132, March 1963.
3. C. A. Balanis and L. Peters, Jr., "Equatorial Plane Pattern of an Axial-TEM Slot on a Finite Size Ground Plane," *IEEE Trans. Antennas Propagat.,* Vol. AP-17, No. 3, pp. 351–353, May 1969.
4. C. A. Balanis, "Pattern Distortion Due to Edge Diffractions," *IEEE Trans. Antennas Propagat.,* Vol. AP-18, No. 4, pp. 551–563, July 1970.
5. C. A. Balanis, "Analysis of an Array of Line Sources Above a Finite Ground Plane," *IEEE Trans. Antennas Propagat.,* Vol. AP-19, No. 2, pp. 181–185, March 1971.
6. D. Proctor, "Graphs Simplify Corner Reflector Antenna Design," *Microwaves,* Vol. 14, No. 7, pp. 48, 52, July 1975.
7. E. B. Moullin, *Radio Aerials,* Oxford University Press, 1949, Chapters 1 and 3.
8. R. E. Paley and N. Wiener, *Fourier Transforms in the Complex Domain,* American Mathematical Society, Providence, R. I., p. 116, 1934.
9. P. A. J. Ratnasiri, R. G. Kouyoumjian, and P. H. Pathak, "The Wide Angle Side Lobes of Reflector Antennas," ElectroScience Laboratory, The Ohio State University, Technical Report 2183-1, March 23, 1970.
10. G. L. James and V. Kerdemelidis, "Reflector Antenna Radiation Pattern Analysis by

Equivalent Edge Currents," *IEEE Trans. Antennas Propagat.*, Vol. AP-21, No. 1, pp. 19–24, January 1973.

11. C. A. Mentzer and L. Peters, Jr., "A GTD Analysis of the Far-out Side Lobes of Cassegrain Antennas," *IEEE Trans. Antennas Propagat.*, Vol. AP-23, No. 5, pp. 702–709, September 1975.

12. L. M. LaLonde and D. E. Harris, "A High Performance Line Source Feed for the AIO Spherical Reflector," *IEEE Trans. Antennas Propagat.*, Vol. AP-18, No. 1, pp. 41–48, January 1970.

13. A. W. Rudge, "Offset-Parabolic-Reflector Anennas: A Review," *Proc. IEEE*, Vol. 66, No. 12, pp. 1592–1618, December 1978.

14. P. J. B. Clarricoats and G. T. Poulton, "High-Efficiency Microwave Reflector Antennas—A Review," *Proc. IEEE*, Vol. 65, No. 10, pp. 1470–1502, October 1977.

15. O. Hachenberg, B. H. Grahl, and R. Wielebinski, "The 100-Meter Radio Telescope at Effelsberg," *Proc. IEEE*, Vol. 69, No. 9, pp. 1288–1295, 1973.

16. P. D. Potter, W. D. Merrick, and A. C. Ludwig, "Big Antenna Systems for Deep-Space Communications," *Astronautics and Aeronautics*, pp. 84–95, October 1966.

17. S. Silver (ed.), *Microwave Antenna Theory and Design*, McGraw-Hill, New York, 1949 (MIT Radiation Lab. Series, Vol. 12).

18. J. F. Kauffman, W. F. Croswell, and L. J. Jowers, "Analysis of the Radiation Patterns of Reflector Antennas," *IEEE Trans. Antennas Propagat.*, Vol. AP-24, No. 1, pp. 53–65, January 1976.

19. R. E. Collin and F. J. Zucker (eds.), *Antenna Theory Part II*, McGraw-Hill, New York, 1969, pp. 36–48.

20. P. K. Agrawal, J. F. Kauffman, and W. F. Croswell, "Calculated Scan Characteristics of a Large Spherical Reflector Antenna," *IEEE Trans. Antennas Propagat.*, Vol. AP-27, No. 3, pp. 430–431, May 1979.

21. E. M. T. Jones, "Paraboloid Reflector and Hyperboloid Lens Antennas," *IRE Trans. Antennas Propagat.*, Vol. AP-2, No. 3, pp. 119–127, July 1954.

22. I. Koffman, "Feed Polarization for Parallel Currents in Reflectors Generated by Conic Sections," *IEEE Trans. Antennas Propagat.*, Vol. AP-14, No. 1, pp. 37–40, January 1966.

23. A. W. Love, "Some Highlights in Reflector Antenna Development," *Radio Science*, Vol. 11, Nos. 8, 9, pp. 671–684, August–September 1976.

24. D. K. Cheng, "Effect of Arbitrary Phase Errors on the Gain and Beamwidth Characteristics of Radiation Pattern," *IRE Trans. Antennas Propagat.*, Vol. AP-3, No. 3, pp. 145–147, July 1955.

25. Y. Y. Hu, "A Method of Determining Phase Centers and Its Application to Electromagnetic Horns," *J. Franklin Inst.*, pp. 31–39, January 1961.

26. J. Ruze, "The Effect of Aperture Errors on the Antenna Radiation Pattern," *Nuevo Cimento Suppl.*, Vol. 9, No. 3, pp. 364–380, 1952.

27. H. C. Minnett and B. MacA. Thomas, "Fields in the Image Space of Symmetrical Focusing Reflectors," *Proc. IEE*, Vol. 115, pp. 1419–1430, October 1968.

28. G. F. Koch, "Coaxial Feeds for High Aperture Efficiency and Low Spillover of Paraboloidal Reflector Antennas," *IEEE Trans. Antennas Propagat.*, Vol. AP-21, No. 2, pp. 164–169, March 1973.

29. R. E. Lawrie and L. Peters, Jr., "Modifications of Horn Antennas for Low Side Lobe Levels," *IEEE Trans. Antennas Propagat.*, Vol. AP-14, No. 5, pp. 605–610, September 1966.

30. A. J. Simmons and A. F. Kay, "The Scalar Feed-A High Performance Feed for Large Paraboloid Reflectors," *Design and Construction of Large Steerable Aerials*, IEE Conf. Publ. 21, pp. 213–217, 1966.

31. W. M. Truman and C. A. Balanis, "Optimum Design of Horn Feeds for Reflector Antennas," *IEEE Trans. Antennas Propagat.*, Vol. AP-22, No. 4, pp. 585–586, July 1974.

32. B. Houshmand, B. Fu, and Y. Rahmat-Samii, "Reflector Antenna Analysis Software," Vol. II, Chapter 11, CAEME Center for Multimedia Education, University of Utah, pp. 447–465, 1995.

33. P. W. Hannan, "Microwave Antennas Derived from the Cassegrain Telescope," *IRE Trans. Antennas Propagat.,* Vol. AP-9, No. 2, pp. 140–153, March 1961.

34. W. V. T. Rusch, "Scattering from a Hyperboloidal Reflector in a Cassegrain Feed System," *IEEE Trans. Antennas Propagat.,* Vol. AP-11, No. 4, pp. 414–421, July 1963.

35. P. D. Potter, "Application of Spherical Wave Theory to Cassegrainian-Fed Paraboloids," *IEEE Trans. Antennas Propagat.,* Vol. AP-15, No. 6, pp. 727–736, November 1967.

36. W. C. Wong, "On the Equivalent Parabola Technique to Predict the Performance Characteristics of a Cassegrain System with an Offset Feed," *IEEE Trans. Antennas Propagat.,* Vol. AP-21, No. 3, pp. 335–339, May 1973.

37. V. Galindo, "Design of Dual-Reflector Antennas with Arbitrary Phase and Amplitude Distributions," *IEEE Trans. Antennas Propagat.,* Vol. AP-12, No. 4, pp. 403–408, July 1964.

38. W. F. Williams, "High Efficiency Antenna Reflector," *Microwave Journal,* Vol. 8, pp. 79–82, July 1965.

39. G. W. Collins, "Shaping of Subreflectors in Cassegrainian Antennas for Maximum Aperture Efficiency," *IEEE Trans. Antennas Propagat.,* Vol. AP-21, No. 3, pp. 309–313, May 1973.

40. C. A. Balanis, *Advanced Engineering Electromagnetics,* John Wiley & Sons, Inc., New York, pp. 744–764, 1989.

41. R. Mittra and V. Galindo-Israel, "Shaped Dual Reflector Synthesis," *IEEE Antennas and Propagation Society Newsletter,* Vol. 22, No. 4, pp. 5–9, August 1980.

42. K. A. Green, "Modified Cassegrain Antenna for Arbitrary Aperture Illumination," *IEEE Trans. Antennas Propagat.,* Vol. AP-11, No. 5, pp. 589–590, September 1963.

43. J. Ashmead and A. B. Pippard, "The Use of Spherical Reflectors as Microwave Scanning Aerials," *J. Inst. Elec. Eng.,* Vol. 93, Part III-A, pp. 627–632, 1946.

44. T. Li, "A Study of Spherical Reflectors as Wide-Angle Scanning Antennas," *IRE Trans. Antennas Propagat.,* Vol. AP-7, No. 3, pp. 223–226, July 1959.

45. R. C. Spencer, C. J. Sletten, and J. E. Walsh, "Correction of Spherical Aberration by a Phased Line Source," *Proceedings National Electronics Conference,* Vol. 5, pp. 320–333, 1949.

46. A. C. Schell, "The Diffraction Theory of Large-Aperture Spherical Reflector Antennas," *IEEE Trans. Antennas Propagat.,* Vol. AP-11, No. 4, pp. 428–432, July 1963.

PROBLEMS

15.1. An infinite line source, of constant electric current I_0, is placed a distance s above a flat and infinite electric ground plane. Derive the array factor.

15.2. For corner reflectors with included angles of $\alpha = 60°, 45°,$ and $30°$:

(a) Derive the array factors of (15-7)–(15-9b).

(b) Plot the field strength along the axis ($\theta = 90°, \phi = 0°$) as a function of the feed-to-vertex spacing, $0 \leq s/\lambda \leq 10$.

15.3. Consider a corner reflector with an included angle of $\alpha = 36°$.

(a) Derive the array factor.

(b) Plot the relative field strength along the axis ($\theta = 90°, \phi = 0°$) as a function of the feed-to-vertex spacing s, for $0 \leq s/\lambda \leq 10$.

(c) Determine the spacing that yields the first maximum possible field strength along the axis. For this spacing, what is the ratio of the field strength of the corner reflector along the axis to the field strength of the feed element alone?

(d) For the spacing in part c, plot the normalized power pattern in the azimuthal plane ($\theta = 90°$).

15.4. A 60° corner reflector, in conjunction with a $\lambda/2$ dipole feed, is used in a radar tracking system. One of the requirements for such a system is that the antenna, in one of its modes of operation, has a null along the forward symmetry axis. In order to accomplish this, what should be the feed spacing from the vertex (in wavelengths)? To get credit, give all the possible values of the feed-to-vertex spacing.

15.5. For a parabolic reflector, derive (15-25) which relates the f/d ratio to its subtended angle θ_0.

15.6. Show that for a parabolic reflector
   (a) $0 \leq f/d \leq 0.25$ relates to $180° \geq \theta_0 \geq 90°$
   (b) $0.25 \leq f/d \leq \infty$ relates to $90° \geq \theta_0 \geq 0°$

15.7. The diameter of a paraboloidal reflector antenna (dish), used for public television stations, is 10 meters. Find the far-zone distance if the antenna is used at 2 and 4 GHz.

15.8. Show that the directivity of a uniformly illuminated circular aperture of diameter d is equal to $(\pi d/\lambda)^2$.

15.9. Verify (15-33) and (15-33a).

15.10. The field radiated by a paraboloidal reflector with an f/d ratio of 0.5 is given by

$$E = (\hat{a}_x + \hat{a}_y \sin \phi \cos \phi)\, f(r, \theta, \phi)$$

where the x-component is the co-pol and the y-component is the cross-pol.
   (a) At what observation angle(s) (in degrees) $(0° - 180°)$ is the cross-pol minimum? What is the minimum value?
   (b) At what observation angle(s) (in degrees) $(0° - 180°)$ is the cross-pol maximum? What is the maximum value?
   (c) What is the polarization loss factor when the receiving antenna is linearly polarized in the x-direction.
   (d) What is the polarization loss factor when the receiving antenna is linearly polarized in the y-direction.
   (e) What should the polarization of the receiving antenna be in order to eliminate the losses due to polarization? Write an expression for the polarization of the receiving antenna to achieve this.

15.11. Verify (15-49) and (15-54).

15.12. A small parabolic reflector (dish) of revolution, referred to as a paraboloid, is now being advertised as a TV antenna for direct broadcast. Assuming the diameter of the reflector is 1 meter, determine at 3 GHz the directivity (in dB) of the antenna if the feed is such that
   (a) the illumination over the aperture is uniform (ideal)
   (b) the taper efficiency is 80% while the spillover efficiency is 85%. Assume no other losses. What is the total aperture efficiency of the antenna (in dB)?

15.13. The 140-ft (42.672-m) paraboloidal reflector at the National Radio Astronomy Observatory, Green Bank, W. Va, has an f/d ratio of 0.4284. Determine the
   (a) subtended angle of the reflector
   (b) aperture efficiency assuming the feed pattern is symmetrical and its gain pattern is given by $2 \cos^2 (\theta'/2)$, where θ' is measured from the axis of the reflector
   (c) directivity of the entire system when the antenna is operating at 10 GHz, and it is illuminated by the feed pattern of part (b)
   (d) directivity of the entire system at 10 GHz when the reflector is illuminated by the feed pattern of part (b) and the maximum aperture phase deviation is $\pi/16$ rad

15.14. A paraboloidal reflector has an f/d ratio of 0.38. Determine
   (a) which $\cos^n \theta'$ symmetrical feed pattern will maximize its aperture efficiency
   (b) the directivity of the reflector when the focal length is 10λ
   (c) the value of the feed pattern in dB (relative to the main maximum) along the edges of the reflector

15.15. Verify that the ideal parabolic reflector feed pattern, for uniform amplitude taper and no spillover, is that represented by $\sec^4 (\theta'/2)$.

15.16. The symmetrical feed pattern for a paraboloidal reflector is given by

$$G_f = \begin{cases} G_0 \cos^4\left(\dfrac{\theta'}{2}\right) & 0 \le \theta' \le \pi/2 \\ 0 & \text{elsewhere} \end{cases}$$

where G_0 is a constant.

(a) Evaluate the constant G_0.

(b) Derive an expression for the aperture efficiency.

(c) Find the subtended angle of the reflector that will maximize the aperture efficiency. What is the maximum aperture efficiency?

15.17. A paraboloidal reflector is operating at a frequency of 5 GHz. It is 8 meters in diameter, with an f/d ratio of 0.25. It is fed with an antenna whose primary pattern is symmetrical and which can be approximated by

$$G_f = \begin{cases} 10 \cos^4 \theta' & 0 \le \theta' \le \pi/2 \\ 0 & \text{elsewhere} \end{cases}$$

Find its

(a) aperture efficiency

(b) overall directivity

(c) spillover efficiency

(d) taper efficiency

15.18. A parabolic reflector has a diameter of 10 meters and has an included angle of $\theta_0 = 30°$. The directivity at the operating frequency of 25 GHz is 5,420,000. The phase efficiency, polarization efficiency, blockage efficiency, and random error efficiency are all 100%. The feed has a phi-symmetric pattern given by

$$G_f = \begin{cases} G_0 \cos^{10} \theta' & 0° \le \theta' \le 90° \\ 0 & \text{elsewhere} \end{cases}$$

Find the taper, spillover, and overall efficiencies.

15.19. A 10-meter diameter paraboloidal reflector is used as a TV satellite antenna. The focus-to-diameter ratio of the reflector is 0.536 and the pattern of the feed in the forward region can be approximated by $\cos^2(\theta')$. Over the area of the reflector, the incident power density from the satellite can be approximated by a uniform plane wave with a power density of 10 μ watts/m². At a center frequency of 9 GHz:

(a) What is the maximum directivity of the reflector (in dB)?

(b) Assuming no losses of any kind, what is the maximum power that can be delivered to a TV receiver connected to the reflector through a lossless transmission line?

15.20. A 3-meter diameter parabolic reflector is used as a receiving antenna for satellite television reception at 5 GHz. The reflector is connected to the television receiver through a 78-ohm coaxial cable. The aperture efficiency is approximately 75%. Assuming the maximum incident power density from the satellite is 10 microwatts/square meter and the incident wave is polarization-matched to the reflector antenna, what is the:

(a) Directivity of the antenna (in dB)

(b) Maximum power (in watts) that can be delivered to the receiving TV? Assume no losses.

(c) Power (in watts) delivered to the receiving TV if the reflection coefficient at the transmission line/receiving TV terminal junction is 0.2. Assume no other losses.

15.21. A reflector antenna with a total subtended angle of 120° is illuminated at 10 GHz with a specially designed feed so that its aperture efficiency is nearly unity. The focal distance of the reflector is 5 meters. Assuming the radiation pattern is nearly symmetric, determine the:

(a) Half-power beamwidth (in degrees).

(b) Sidelobe level (in dB).

(c) Directivity (in dB).

(d) Directivity (in dB) based on Kraus' formula and Tai & Pereira's formula.

(e) Loss in directivity (in dB) if the surface has rms random roughness of 0.64 mm.

15.22. A front-fed paraboloidal reflector with an f/d radio of 0.357, whose diameter is 10 meters and which operates at 10 GHz, is fed by an antenna whose power pattern is rotationally symmetric and it is represented by $\cos^2(\theta/2)$. All the power is radiated in the forward region ($0° \leq \theta' \leq 90°$) of the feed. Determine the

(a) spillover efficiency

(b) taper efficiency

(c) overall aperture efficiency

(d) directivity of the reflector (in dB)

(e) directivity of the reflector (in dB) if the RMS, reflector surface deviation from an ideal paraboloid is $\lambda/100$.

15.23. Design pyramidal horn antennas that will maximize the aperture efficiency or produce maximum power transmission to the feed, for paraboloidal reflectors with f/d ratios of

(a) 0.50

(b) 0.75

(c) 1.00